RSC Advances

PAPER

View Article Online
View Journal | View Issue

Cite this: *RSC Adv.*, 2026, **16**, 22969

First-principles study of rare-earth-free Cs_4SrI_6:Tl, a zero-dimensional halide perovskite for scintillation applications

Md. Helal Miah, [ab] Mayeen Uddin Khandaker, [*acd] Yahaya Saadu Itas, [ae] Amran Hossain,[f] Phannee Saengkaew, [g] Arshid Numan,[h] Mohammad Aminul Islam[ij] and Mohammad Nur-E-Alam[k]

In recent years, rare-earth-activated perovskite scintillators have drawn significant research attention owing to their characteristic and efficient $4f^n \leftrightarrow 4f^{n-1}5d$ electronic transitions. However, the high cost and limited readiness of rare-earth elements motivate the search for alternative activators. In this context, thallium ions (Tl^+) can offer a promising activator that can act as a two-level luminescent center, yielding characteristic emissions through $6s^16p^1 \rightarrow 6s^2$ electronic transitions, similar to the well-known NaI:Tl scintillator while remaining cost-effective. In this investigation, density functional theory (DFT) calculations were performed to explore the opto-electronic and scintillation–relevant properties of the undoped and Tl^+-doped Cs_4SrI_6 halide perovskites. The computed band structures demonstrated the reduction of band gap with the increasing Tl^+ concentrations. The observed relatively flat bands near the band edges suggested large carrier effective masses, which may suppress carrier mobility and promote carrier localization. In halide systems with strong electron-phonon coupling, such localization can lead to the formation of self-trapped excitons that may recombine radiatively through Tl^+ activator centers, enhancing the emission efficiency. More specifically, Tl^+ introduces localized Tl^+-6s* and Tl^+-6p* states above valence band maximum (VBM) and below conduction band minimum (CBM) of the host Cs_4SrI_6, respectively. As the Tl^+ concentration increases, these states (especially Tl^+-6s*) become more prominent and enhance the probability of efficient and characteristic radiative emission from Tl^+-$6p^*(6s^16p^1) \rightarrow Tl^+$-$6s^*$ ($6s^2$). urthermore, the estimated values of radiant quantum efficiency were 39.52%, 41.41%, and 43.70% for Cs_4SrI_6 doped with 1.52% Tl^+, 3.03% Tl^+, and 4.55% Tl^+, respectively, which showed enhanced energy conversion efficiency. Additionally, the reduction in band gap with the increasing Tl^+ concentration led to an increase in the theoretical upper limit of light yield (LY), exceeding 108 401 photons/MeV for the 4.55% Tl^+ dopant under ideal conditions. Moreover, this investigation revealed an Auger-free luminescence process in Tl^+-doped compounds, which reduced self-absorption losses. These results demonstrated that Tl^+ in Cs_4SrI_6 offers a cost-effective and rare-earth-free alternative activator for perovskite-based scintillators, with the favorable characteristics of light emission and promising scintillation performance.

Received 31st January 2026
Accepted 12th April 2026

DOI: 10.1039/d6ra00836d

rsc.li/rsc-advances

[a]*Applied Physics and Radiation Technologies Group, CCDCU, Faculty of Engineering and Technology, Sunway University, Bandar Sunway, Selangor, 47500, Malaysia. E-mail: mu_khandaker@yahoo.com; mayeenk@diu.edu*

[b]*Department of Physics, Gopalganj Science and Technology University, Gopalganj-8105, Bangladesh*

[c]*Faculty of Graduate Studies, Daffodil International University, Daffodil Smart City, Birulia, Savar, Dhaka-1216, Bangladesh*

[d]*Department of Physics, College of Science, Korea University, 145 Anam-ro, Seongbuk-gu, Seoul, 02841, Republic of Korea*

[e]*Department of Physics, Saadu Zungur University, Gadau, Nigeria*

[f]*Department of Information and Electronic Engineering, Muroran Institute of Technology, Muroran, 050-8585, Japan*

[g]*Department of Nuclear Engineering, Faculty of Engineering, Chulalongkorn University, Bangkok 10330, Thailand*

[h]*Sunway Centre for Electrochemical Energy and Sustainable Technology, Faculty of Engineering and Technology, Sunway University, Bandar Sunway, Selangor, 47500, Malaysia*

[i]*Department of Electrical Engineering, Faculty of Engineering, Universiti Malaya, Jalan Universiti, 50603 Kuala Lumpur, Malaysia*

[j]*Miyan Research Institute, International University of Business Agriculture and Technology, Dhaka, 1230, Bangladesh*

[k]*Space Science Centre, Institute of Climate Change, Universiti Kebangsaan Malaysia, Bangi 43600, Selangor, Malaysia*

1 Introduction

Phosphor materials absorb incident high-energy radiation and efficiently convert the absorbed energy into lower-energy light (most commonly ultraviolet or visible light); this phenomenon is called luminescence. For any phosphor, two properties are critical: absorption efficiency and light output. The absorption efficiency is primarily determined by the effective atomic number of the constituent elements; phosphors contain high-Z_{eff} elements, which enable the effective absorption of high energy.[1–3] Light output depends on factors such as the conversion efficiency, the electronic band gap, and the optical transparency of the phosphor to its own emitted light. Among various phosphors, CsI:Tl, NaI:Tl, SrI_2:Eu, $CdWO_4$, and BGO are prominent.[4] However, their energy resolution still lags behind that of semiconductor detectors, especially HPGe.[5] Commercially, BGO, $CdWO_4$, CsI:Tl, and NaI:Tl scintillators are utilized in high-energy radiation detection. Nevertheless, along with resolution, they suffer from low light production ($CdWO_4$ and BGO), high afterglow (CsI:Tl) and hygroscopicity (NaI:Tl).[6] Therefore, it is indispensable to explore novel materials to substitute traditional materials for ionizing radiation sensing.

The most studied binary materials for scintillation are alkaline earth metal halides (*e.g.* $BX_2 = SrI_2$) and alkali metal halides (*e.g.* AX = CsI). In recent years, the superior scintillation performance of these materials compared with the existing scintillators has inspired the research community to decipher performances from the stoichiometric combination of both halide materials that can synergistically combine the intrinsic benefits of each halide class. In addition, the mixture of these two halide compounds with different ratios yields a number of dimensional perovskite compounds presenting a variety of structural configurations, containing $AX:BX_2 = ABX_3$ (3D), $2AX:BX_2 = A_2BX_4$ (2D), $AX:2BX_2 = AB_2X_5$ (2D) and $4AX:BX_2 = A_4BX_6$ (0D) frameworks.[7–12] Due to the highest effective atomic number and quantum effect of the zero-dimensional (0D) structure among its counterparts, it naturally attracts interest as a promising candidate for scintillator applications. In an endeavor to progress 0D perovskite compounds, the famous research team led by Stand had grown a Cs_4CaI_6:4%Eu scintillator employing the Bridgman–Stockbarger technique and calculated its scintillation performance.[13] They confirmed an LY of 51 800 photons/MeV and an ER of 3.6% when the scintillator was subjected to gamma rays from a ^{137}Cs source. To further augment the device performance, they adopted compositional engineering *via* replacing calcium with strontium. This adjustment led to significant advances of the device Cs_4SrI_6:4%Eu performance metrics with a higher LY of 62 300 photons per MeV along with an improved ER of 3.3%. These results emphasize the promise of these compounds for high-resolution γ-ray spectroscopy and Cs_4SrI_6:4%Eu arising as a promising scintillator. Subsequently, Rutstrom *et al.* investigated the influences of europium ion (Eu^{2+}) concentration on the scintillation performance of Cs_4SrI_6 under the ^{137}Cs source.[14] With the increase in Eu^{2+} dopant concentration from 0.5% to 7% in Cs_4SrI_6, the performance metrics, especially LY, increased from 23 000 photons/MeV to 71 000 photons per MeV and the energy resolution changed from 6.6% to 3.2%. These outcomes reveal that the LY augments due to additional activators, which essentially enhance the radiation recombination pathway. However, the dopant concentration should be optimized; otherwise, it would act as a self-absorber at higher concentrations. In subsequent research, ytterbium was introduced as a new dopant at various concentrations, and its performance was evaluated under a ^{137}Cs source.[15] The study revealed that the Cs_4SrI_6 scintillator with 3% Yb^{2+} attained an LY of 40 000 photons per MeV, and an optimal resolution of 5.1% was achieved for 1% Yb^{2+}. However, so far, only a few studies have been reported on Sr-based zero-dimensional perovskites (Cs_4SrI_6). Extensive research is needed because of their promising performance compared to conventional scintillators (CsI:Tl demonstrates an ER of 4.42% to 6%[16–18] and NaI:Tl shows an ER of 6.5% to 7% under a ^{137}Cs source).[19,20]

Moreover, emission tunability and LY enhancement can be accomplished by integrating suitable dopant ions into the host matrix. However, research on perovskite-based scintillators is mostly limited by a narrow attention on a small number of dopants, predominantly europium, with only a few studies exploring samarium and ytterbium ions as activators for their well-defined characteristic emissions.[4] However, the high material cost ($EuI_2 \sim 300$ USD per g) and readiness of rare-earth elements present practical constraints for large-scale exploitation. Furthermore, thallium ion (Tl^+), widely recognized as the benchmark activator in commercially dominant scintillators, for instance, NaI:Tl and CsI:Tl, has not yet been systematically explored within the various dimensional perovskites. Additionally, the Tl^+ compound remains relatively inexpensive (approximately TlI ~8 USD per gram; source: Sigma-Aldrich), making it an economically attractive candidate as a dopant material. To date, no theoretical or experimental investigations have explored the development of scintillators based on Tl^+-doped zero-dimensional perovskites derived from alkali and alkaline earth metal halides, highlighting a significant gap in the field.

This work contributes to the advancement of perovskite-based scintillation research by providing a theoretical understanding of the activator behavior of thallium ions (Tl^+) in the OD structure Cs_4SrI_6 by means of DFT for the first time. By elucidating whether Tl^+ acts as a single-level or two-level activator, this study offers valuable insights into the mechanisms governing radiative recombination and energy transfer processes in perovskites. In particular, efficient radiative transitions associated with the de-excitation of the Tl^+ ion occur only if both the Tl^+-6p* state and the Tl^+-6s* state lie within the band gap of the host compound. Under these conditions, the electronic transition occurs between localized states (Tl^+-$6p^*(6s^16p^1) \rightarrow Tl^+$-$6s^*(6s^2)$) of the activator ion and Tl^+ behaves as a two-level activator, resulting in a characteristic and single narrow peak emission like rare earth activator ions (Eu^{2+}). In contrast, single-level activators exhibit a broad emission spectrum, in which only the Tl^+-6p* state is located in the host band gap, typically arising from the Tl^+-bound excitonic or defect-related transitions, such as Tl^+-6p* → V_k emission. By

understanding the electronic transition mechanisms, this study provides guidance for the design of a high-performance perovskite scintillator with thallium ions as the activator.

2 Methodology

Density functional theory enables the theoretical prediction of a phosphor material's properties, including optoelectronic, thermodynamic and mechanical properties, by computing its ground-state structure with basic input parameters. The primary requirements are the crystal structure and the atomic numbers of the constituent elements, while other computational parameters can be selected as needed. Once the total energy of the ground state of system has been determined, various opto-electronic properties including band structures, densities of states, and dielectric function, $\varepsilon(\omega)$, can be obtained.[21] The Quantum ESPRESSO package is one of several computational tools that implement DFT for optoelectronic, thermodynamic and mechanical properties that can be calculated.[22]

The compound Cs_4SrI_6 belongs to the trigonal crystal system with an $R\bar{3}c$ space group.[13] Although this structure belongs to the rhombohedral lattice system, it is often described using the hexagonal and trigonal p setting, which provides a more convenient coordinate system.[13,23] Trigonal is a subgroup of the hexagonal crystal family. A primitive cell contains 22 atoms, and a conventional cell contains 66 atoms. For the doped structures, Tl^+ substitution was introduced at the Cs^+ lattice site because both ions share the same valence state and comparable ionic radius, making this site energetically favorable for substitution. Systematically, a representative Cs^+ site in the conventional cell was replaced by 1.52%, 3.03% and 4.55% of Tl^+ at the coordinates of (2.724, 3.574, 7.449), (−0.014, 8.344, 7.400) and (2.997, 4.512, 13.579), respectively, to decipher the change of band structure and role of Tl^+ to determine the emission source from these doped structures. The structures were then fully relaxed to obtain the optimized geometry used for subsequent electronic and optical property calculations.

All ground-state calculations were performed using the Quantum ESPRESSO package based on density functional theory. The exchange–correlation interaction was described by using the Generalized Gradient Approximation with the Perdew–Burke–Ernzerhof functional.[24,25] Norm-conserving pseudopotentials, generated using the Martins–Troullier pseudopotential scheme, were used to represent the electron–ion interactions. Electronic convergence was achieved using density mixing, while structural optimization was carried out using the BFGS algorithm until the forces and total energy satisfied the convergence criteria. However, spin–orbit coupling was not explicitly included in the present calculations. Since the investigated system is non-magnetic, spin polarization was also not considered.

Based on systematic convergence tests, a plane-wave kinetic energy cutoff of 80 Ry was adopted for all calculations. In addition, the Brillouin-zone integration was performed using a 4 × 4 × 4 Monkhorst–Pack k-point mesh, which was found

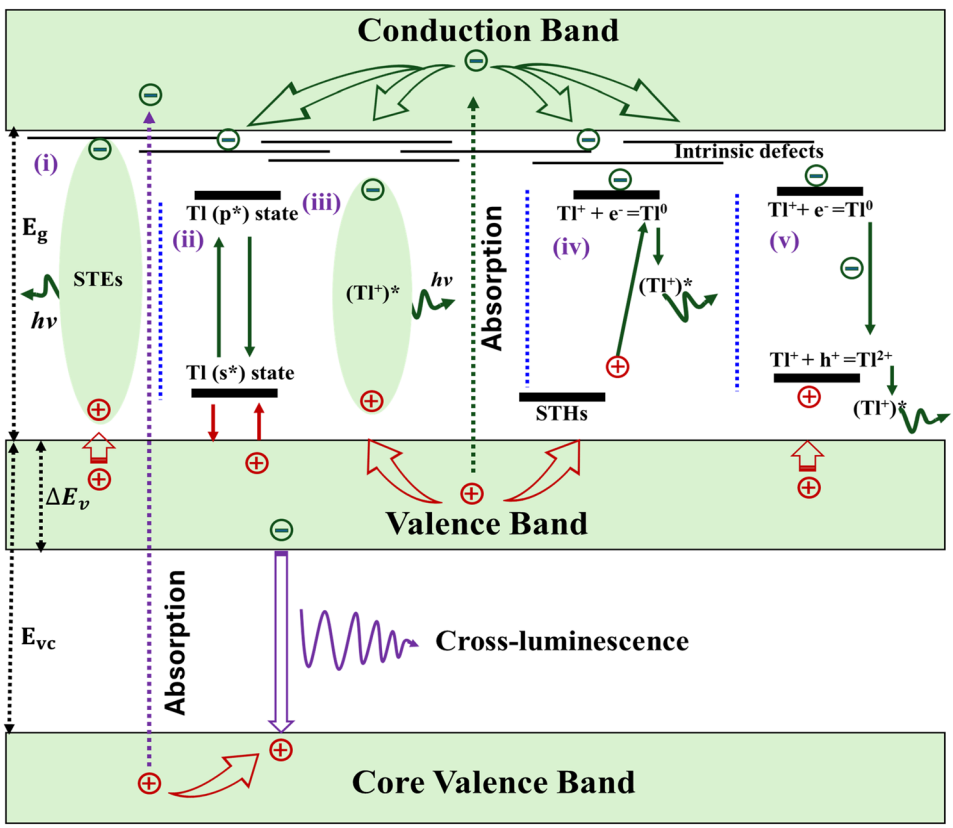

Fig. 1 Illustration of the luminescence mechanisms of the Tl^+-doped two-level activator system and cross-luminescence.

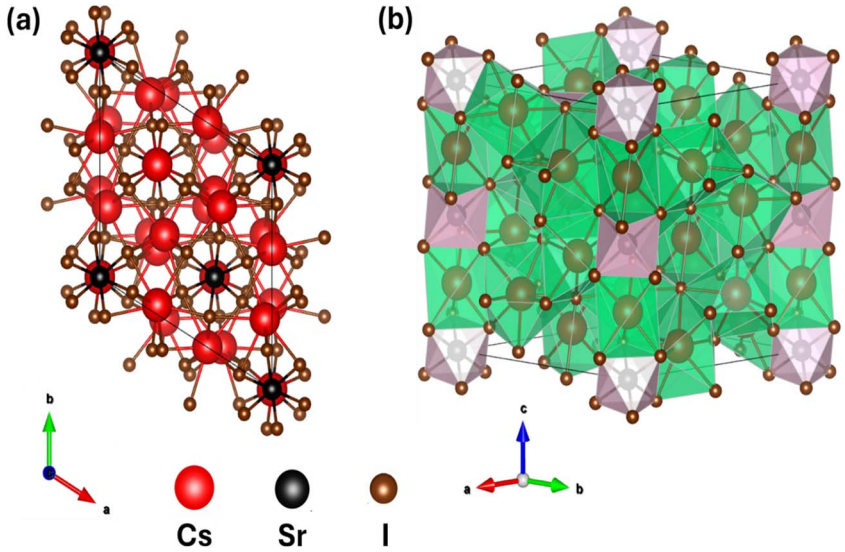

Fig. 2 Conventional representation of the Cs_4SrI_6 compound: (a) crystal structure projections along the (a) *c*-axis (b) *a*-axis, where the rose-pink shaded polyhedral represents $[SrI_6]^{4-}$ octahedra.

sufficient to achieve total-energy convergence for the investigated systems.

The optical properties were calculated from the frequency-dependent complex dielectric function obtained within the independent-particle approximation by using the linear-response formalism employed in the Quantum ESPRESSO package.[22,26,27] Particularly, the independent-particle approximation within the Quantum ESPRESSO package is commonly determined by employing the epsilon.x post-processing code. This approach calculates the frequency-dependent complex dielectric function based on the electronic band structure obtained from a ground-state pw.x calculation. Specifically, the imaginary part of the dielectric function was calculated from interband electronic transitions between occupied and unoccupied states derived from the computed band structure, while the real part was obtained through the Kramers–Kronig relations.[28] From the resulting dielectric function, other optical properties such as the absorption coefficient and refractive index were subsequently derived.

Since pure and Tl^+-doped Cs_4SrI_6 compounds are intended for use in scintillation applications, our analysis is only focused on the optoelectronic properties that directly influence scintillation performance, including charge-carrier dynamics, scintillation efficiency and light yield.

3 Results and discussion

3.1 Structural properties

The structural analysis reveals that the compound Cs_4SrI_6 belongs to the trigonal crystal system with an $R\bar{3}c$ space group.[13] However, it is better to illustrate it using the conventional cell, which provides a more convenient coordinate system. In Cs_4SrI_6, there are two crystallographically independent sites of Cs^+.[23] In the first Cs^+ site, Cs^+ is bonded to six equivalent I^- atoms. All Cs–I bonds are of equal length, 3.7 Å. In the second Cs^+ site, Cs^+ is bonded to eight equivalent I^- atoms. In this case, there is an increase in the Cs–I bond length varying from 3.85 Å to 3.99 Å. In addition, Sr^{2+} is bonded in an octahedral geometry to six equivalent I^- atoms and all Sr–I bonds are of equal length of 3.23 Å. Moreover, I^- is bonded to five Cs^+ and one Sr^{2+} atom to form a mixture of distorted corner, edge, and face-sharing ICs_5Sr octahedra. The structure Cs_4SrI_6 can be illustrated as

Table 1 Structural, electronic, and scintillation performance features of pure Cs_4SrI_6 and the Tl^+-doped Cs_4SrI_6 perovskites

	Lattice parameter in Å			Bond length in Å								
Compound	*a*	*b*	*c*	Cs–I (site 1)	Cs–I (site 2)	Sr–I	Tl–I (1)	Tl–I (2)	Tl–I (3)	Band gap in eV	Radiant quantum efficiency (QE in %)	LY photons per MeV
Cs_4SrI_6	14.37	14.37	17.88	3.7	3.85–3.99	3.23	—	—	—	4.11	—	97 324
Cs_4SrI_6: 1.52%Tl	14.31	14.31	17.86	3.70–3.74	3.82–3.99	3.21–3.24	3.71–3.83	—	—	3.98	39.52	100 503
Cs_4SrI_6: 3.03%Tl	14.32	14.32	17.72	3.66–3.69	3.79–3.99	3.21–3.24	3.45–3.79	3.50–3.53	—	3.90	41.41	102 564
Cs_4SrI_6: 4.55%Tl	14.31	14.31	17.71	3.67–3.73	3.79–3.96	3.22–3.25	3.35–3.87	3.42–3.56	3.34–3.88	3.69	43.70	108 401

a 0D perovskite because the $[SrI_6]^{4-}$ octahedra are isolated from each other.[23] These isolated and slightly distorted $[SrI_6]^{4-}$ octahedra are coordinated with Cs ions along *c*-axis, forming one-dimensional spiral chains of alternating $[SrI_6]^{4-}$ octahedra by face-sharing with distorted $[CsI_6]^{5-}$ trigonal (as shown in Fig. 2(b)).

The lattice parameters of pure Cs_4SrI_6 were estimated at $a = b = 14.37$ Å and $c = 17.88$ Å. Upon Tl^+ doping at the position of Cs^+ in the pure structure, the lattice constants demonstrate noticeable variations due to the difference in ionic radii between Tl^+ and Cs^+. More specifically, the optimized lattice constants were $a = b = 14.31$ Å and $c = 17.86$ Å for 1.52% Tl^+ doping, $a = b = 14.32$ Å and $c = 17.72$ Å for 3.03% Tl^+ doping, and $a = b = 14.305$ Å and $c = 17.71$ Å for 4.55% Tl^+ doping in the pure Cs_4SrI_6 compound. In addition to the lattice contraction, Tl^+ incorporation induces local structural distortions, leading to variations in bond lengths, which are summarized in Table 1. However, due to the lack of available experimental and theoretical data, the present findings could not be corroborated.

3.2 Electronic properties

In materials science, the band structure represents the distribution of allowed electronic energy states and the energy gaps among them, and it is a key factor in controlling the material's electrical and optical responses.[29–31] More specifically, luminescence resulting from the excitation and de-excitation processes of carriers is intricately linked with its band formation. An in-depth analysis of the electronic features of undoped and Tl^+-doped Cs_4SrI_6 was conducted to explore the fundamental photophysical mechanisms, which are responsible for the luminescence spectrum of the scintillator. More specifically, this section involves an extensive computational exploration of the band structure, DOS (density of states), and PDOS (partial density of states) to decipher how orbitals interact and participate in shaping the electronic band. In addition, this analysis elucidates the probable electronic transition associated with characteristic emission. The asymmetric electronic band structures of the conventional cell of Cs_4SrI_6 were studied by adopting a high symmetry path of *k*-point Γ–M–K–Γ–A–L–H–A|L–M|K–H in the Brillouin zone. The band diagram (in Fig. 3–5), DOS (in Fig. 6) and PDOS (in Fig. 7–11) of the pure and doped structures are depicted.

In our calculation, the Fermi energies for pure Cs_4SrI_6, Cs_4SrI_6:1.52%Tl, Cs_4SrI_6:3.03%Tl and Cs_4SrI_6:4.55%Tl compounds were anticipated at ~1.9624 eV, ~1.9400 eV, ~1.9288 eV, and 1.9098 eV, respectively. Alternatively, the Fermi level shifted toward VB (shown in Fig. 3). The Fermi level closer to the VB means that Tl^+ performs as an acceptor-like activator that promotes efficient charge carrier trapping and radiative recombination, which are essential for strong scintillation emissions.

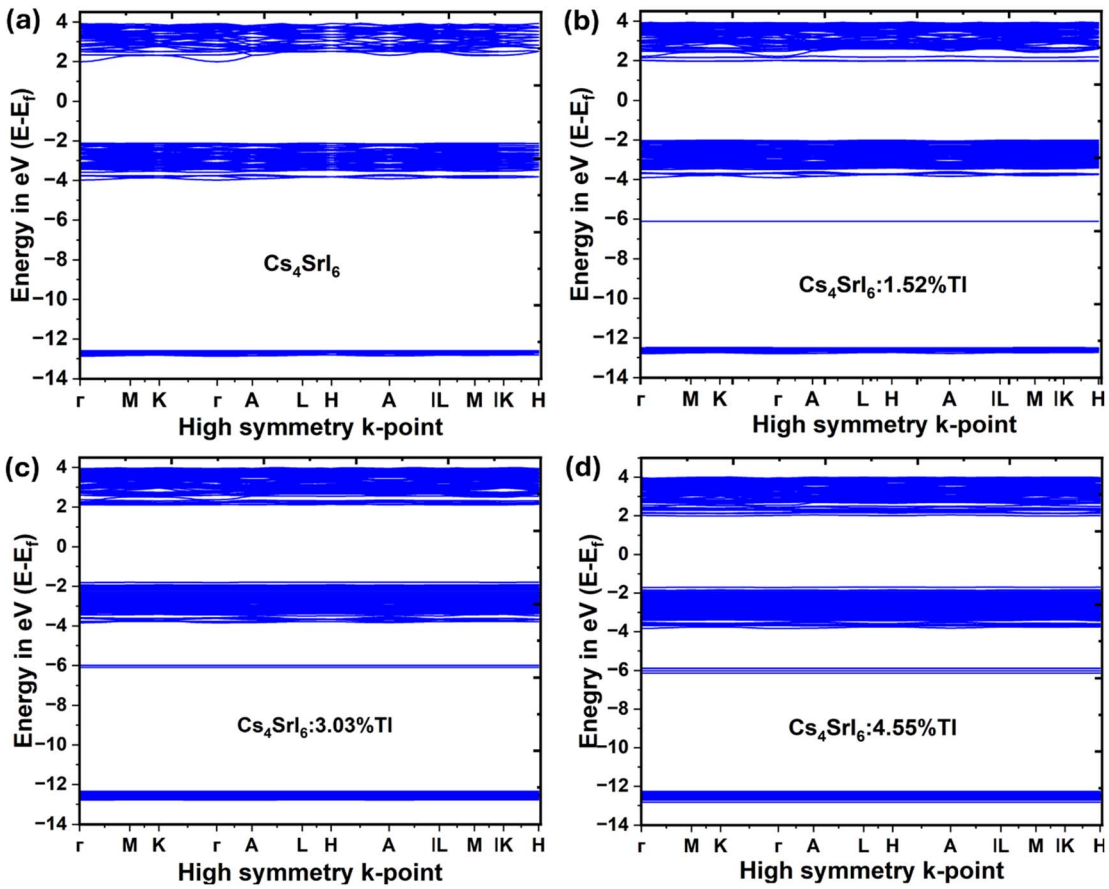

Fig. 3 Band structures of (a) pure Cs_4SrI_6, (b) Cs_4SrI_6 doped with 1.52% Tl^+, (c) Cs_4SrI_6 doped with 3.03% Tl^+, and (d) Cs_4SrI_6 doped with 4.55% Tl^+.

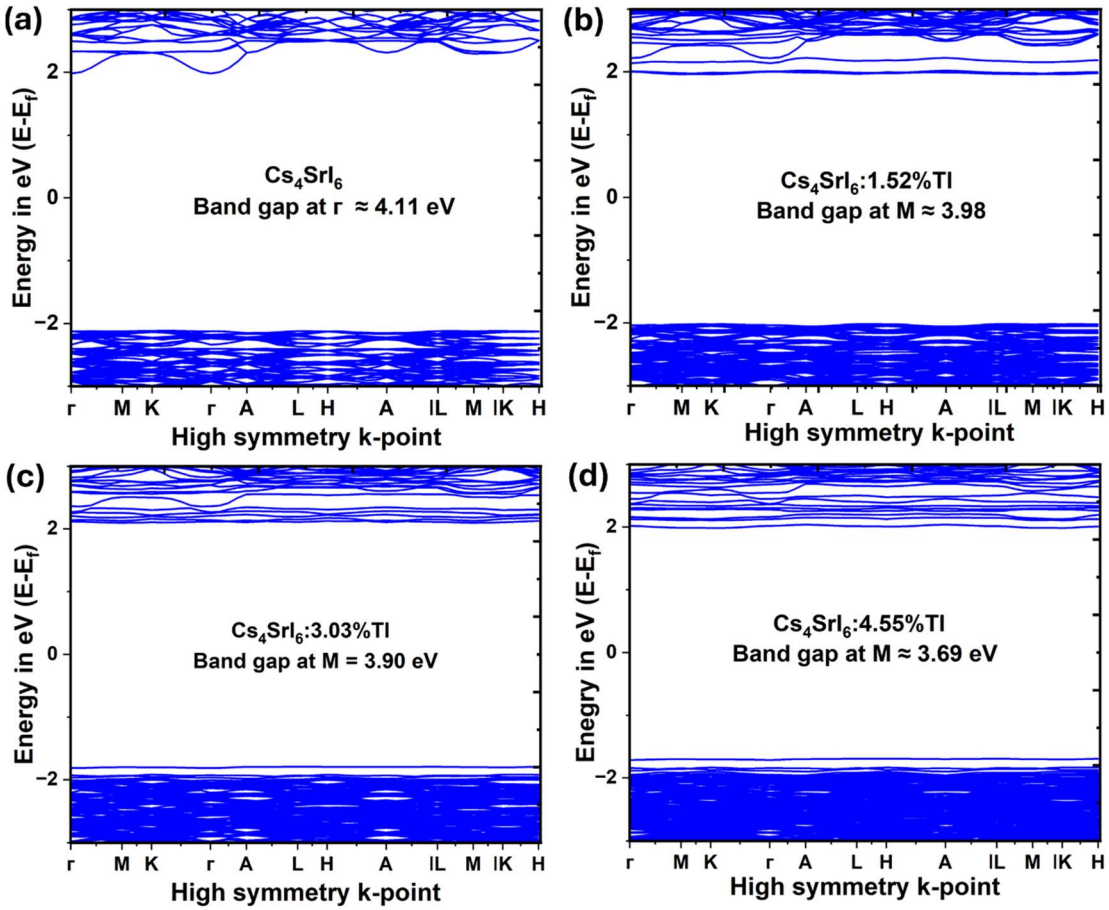

Fig. 4 Visualization of the electronic band gaps illustrating the relative positions of the CBs and VBs of (a) pure Cs_4SrI_6, (b) Cs_4SrI_6 doped with 1.52% Tl^+, (c) Cs_4SrI_6 doped with 3.03% Tl^+, and (d) Cs_4SrI_6 doped with 4.55% Tl^+.

As the emitted photon's energy is nearly comparable to the energy of the bandgap, this observation necessarily emphasizes the bandgap as a crucial feature, which governs the scintillation performance of the material. The electronic band structure of pure Cs_4SrI_6 displays a CBM and VBM at 1.98 eV and −2.13 eV, respectively. Upon doping with Tl^+, shifts of CBM and VBM were observed. For 1.52% Tl^+-doped Cs_4SrI_6, the CBM at 1.96 eV and VBM at −2.02 eV were shifted, which signifies a decrease in the band gap. Likewise, for a 3.03% Tl^+ dopant concentration, the CBM is located at 2.10 eV, whereas the VBM moves to 1.80 eV. Lastly, with a doping concentration of 4.55% Tl^+, the VBM and CBM were located at −1.70 eV and 1.99 eV, respectively. Therefore, Tl^+ doping causes alteration in the band formation, which is expected to significantly influence both the optical characteristics and the scintillation behavior.

This band structure modification occurs due to the arising of new energy states below CBM and above VBM from the contribution of Tl^+. Finally, the bandgaps were estimated at 4.11 eV, 3.98 eV, 3.90 eV and 3.69 eV for Cs_4SrI_6, Cs_4SrI_6:1.52%Tl, Cs_4SrI_6:3.03%Tl, and Cs_4SrI_6:4.55%Tl, respectively (shown in Fig. 4), which are less than those of the constituent binary compounds of SrI_2 (5.5 eV) and CsI (4.95 eV).[32,33] However, it was unable to validate the band gap for pure and Tl^+-doped Cs_4SrI_6 owing to inadequate available data. Additionally, a direct bandgap for pure and doped structures was anticipated. The altered band gap energy is greater than the visible light energy (from 3800 Å (∼3.26 eV) to 7500 Å (∼1.65 eV)); therefore, the likelihood of reabsorption of the emitted visible scintillation light is significantly reduced. In addition, dopant inclusion allows precise tuning of the scintillation emission to ensure compatibility with the spectral sensitivity range of PMT tubes.

In multinary compound materials, the conduction and valence bands arise from the hybridization of electronic states contributed by different cations and anions. The lower-energy region of the conduction (valence) band is primarily composed of states originating from more electronegative cations (anions), whereas the higher-energy region is dominated by states from less electronegative cations (anions). If the electronegativity difference between the constituent cations or anions is sufficiently large, the conduction or valence band may even split into distinct sub-bands.[34] Based on the above discussion, Tl has a higher electronegativity than Cs and Sr but a lower electronegativity than I (I: 2.66; Tl: 1.62; Sr: 0.95; Cs: 0.79) (https://sciencenotes.org/list-of-electronegativity-values-of-the-elements/). Therefore, the lower part of the CB and the upper part of the VB are expected to be contributed by

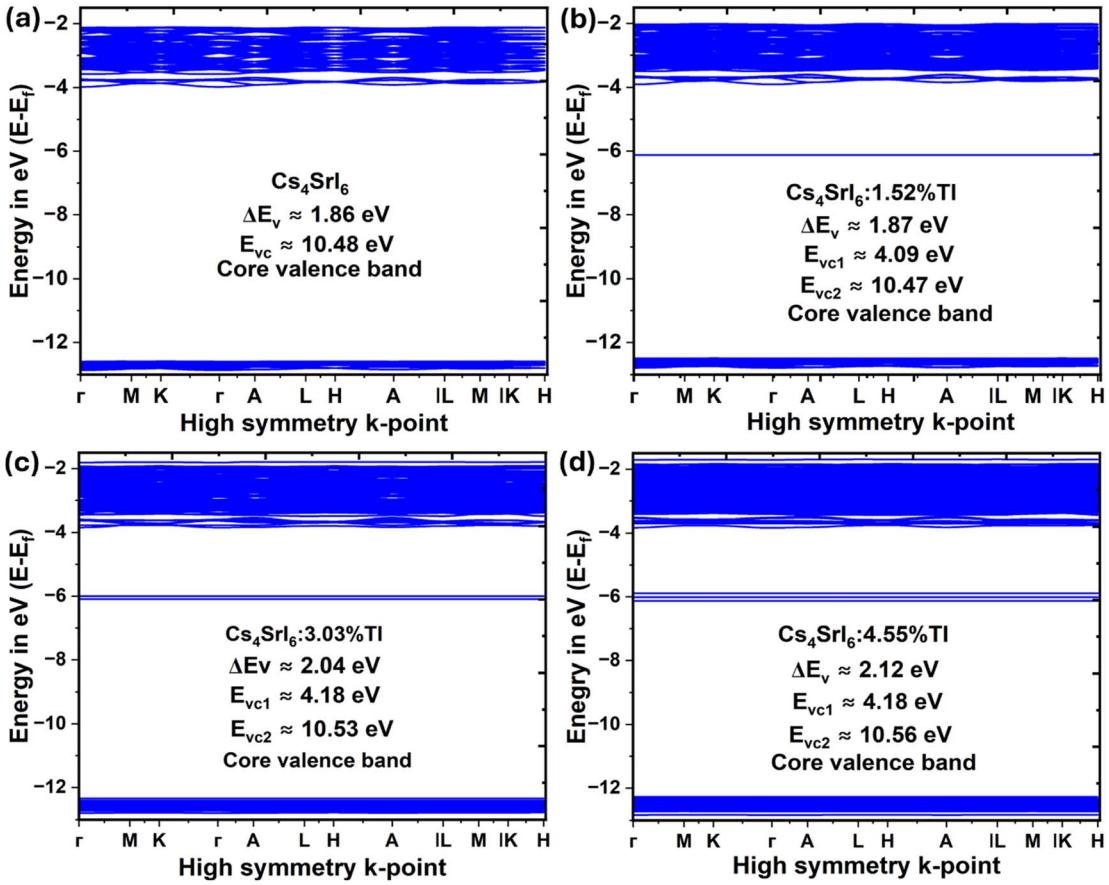

Fig. 5 Visualization of the VBs and core VBs of (a) pure Cs_4SrI_6, (b) Cs_4SrI_6 doped with 1.52% Tl^+, (c) Cs_4SrI_6 doped with 3.03% Tl^+, and (d) Cs_4SrI_6 doped with 4.55% Tl^+.

electronic states originating from Tl^+. The detailed contributions from Tl^+ will be discussed in the PDOS section. Moreover, the pure Cs_4SrI_6 exhibits a moderately dispersive CB and a relatively flat VB, whereas both bands become comparatively flat in all Tl^+-doped compounds. The pure Cs_4SrI_6 compound demonstrated A-type scintillator behavior, satisfying the condition $E_g < E_{vc}$, where E_g denotes the energy of band gap and E_{vc} indicates the energy separation between the top of the core VB and the VBM. In addition, the luminescence from this type of compound is known as Auger luminescence. On the other hand, Tl^+ doped Cs_4SrI_6 exhibited AL-type scintillator behavior because it satisfies the relation $E_g > E_{vc1} - \Delta E_v$, where ΔE_v signifies the width of VB and E_{vc1} means the energy separarition between the top of the first core VB and the VBM (shown in Fig. 5). A detailed analysis of Auger-free and Auger luminescence mechanisms in these scintillators is presented in the section of LY and cross-band luminescence.

The computed band structure of Tl^+-doped Cs_4SrI_6 discloses a highly localized electronic nature, illustrated by weakly dispersive valence and conduction bands throughout the high-symmetry *k*-points. According to eqn (1), the effective mass (m^*) is inversely proportional to the second derivative of energy with respect to the wave vector, where a larger curvature corresponds to a smaller effective mass and *vice versa*[35] as follows:

$$\frac{1}{m^*} = \frac{1}{\hbar^2}\frac{\partial^2 E(k)}{\partial k^2} \quad (1)$$

Since a relatively flat band was observed near the band edges, there is a possibility of obtaining higher effective masses according to eqn (1). A large effective mass can inhibit the free movement of charge carriers, which in turn facilitates the confinement of these carriers. More specifically, the valence band facilitates hole self-trapping, while the similarly flat conduction band supports electron localization.[36] This localization of charge carriers leads to the formation of self-trapped excitons *via* coulombic attraction between electrons and holes. These self-trapped excitons can subsequently undergo radiative recombination *via* Tl^+-mediated luminescence mechanism in Cs_4SrI_6:Tl, potentially enhancing the emission efficiency.

This process may be consistent with the emergence of characteristic emission bands associated with electronic transitions from Tl^+-6p* to Tl^+-6s* states and with the large Stokes shifts commonly reported in Tl^+-activated halide scintillators such as NaI:Tl. The enhanced carrier localization implied by the band structure is therefore expected to improve the light emission efficiency, making this material particularly suitable for scintillation-based radiation detection.

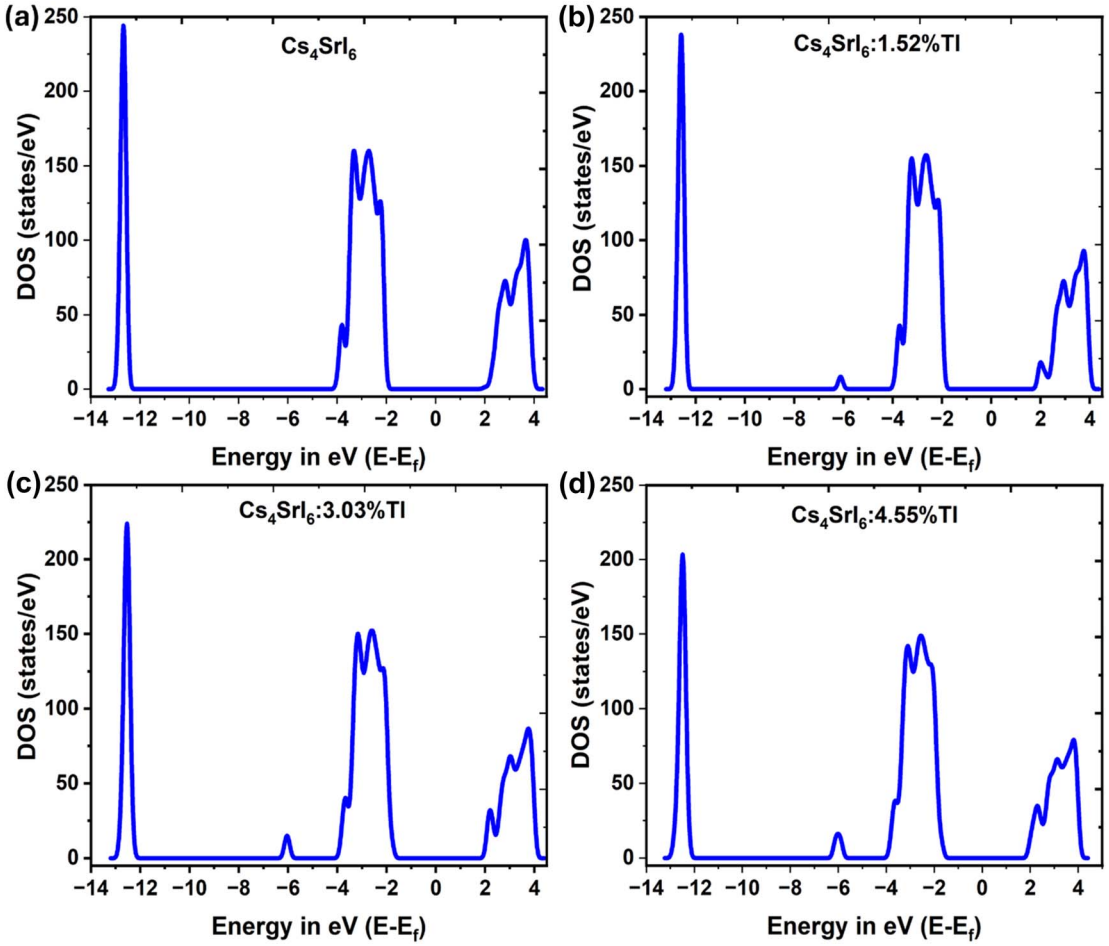

Fig. 6 DOS plots of (a) pure Cs_4SrI_6, (b) Cs_4SrI_6 doped with 1.52% Tl^+, (c) Cs_4SrI_6 doped with 3.03% Tl^+, and (d) Cs_4SrI_6 doped with 4.55% Tl^+.

To obtain a more comprehensive understanding of the band structure of the studied compound, the DOS and PDOS were computed. The analysis of the DOS and PDOS provides valuable insights into the mechanisms governing band formation. Fig. 6–11 display the total DOS and PDOS distributions for pure Cs_4SrI_6, Cs_4SrI_6:1.52%Tl, Cs_4SrI_6:3.03%Tl and Cs_4SrI_6:4.55%Tl, respectively.

In the pure Cs_4SrI_6 structure, the CB extending from 1.98 eV to 3.91 eV predominantly arises from the contribution of the atomic orbitals of Cs^+ and Sr^{2+}. More precisely, the s, p, and d atomic orbitals from Cs^+ and the s and d atomic orbitals from Sr^{2+} contribute to the formation of CB. In addition, the f orbital from both atoms and the d orbital from the I^- atom contribute minimally in the CB. Among all the orbitals, the d atomic orbital from Sr^{2+} plays the most substantial role in shaping the CB. In contrast, the VB originates from the collective participation of the orbitals from all constituent elements in the energy window ranging from −2.12 eV to −3.99 eV. In detail, the s, p, and d atomic orbitals from Cs^+, the s and d atomic orbitals from Sr^{2+}, and the p atomic orbital from I^- involve the construction of VB. Among all these orbitals, the p atomic orbital from I^- plays the most important role in forming the VB. Moreover, the core VB, a narrow band window from −12.60 eV to −12.87 eV, is mainly composed of Cs^+ (s and p), Sr^{2+} (s), and I^- (s). Among all these, the s orbital from I^- makes the most substantial contributions.

As Cs^+ is replaced by Tl^+ with various concentrations, the CB splits into a lower CB and an upper CB. In particular, Tl^+-derived localized states appear just below the CBM, thereby lowering the conduction band edge.

The upper CB is mainly made by the orbitals from Cs^+ (s, p, and d), as well as the orbitals from Sr^{2+} (s and d) like pure Cs_4SrI_6. Conversely, the involvement of the p atomic orbitals from Cs^+ decreases slightly compared to pure Cs_4SrI_6, while the participation of the s atomic orbital from Cs^+ and the d atomic orbitals from Sr^{2+} strengthens. However, the d orbitals from Sr^{2+} lead to the formation of the upper CB. In contrast, the lower CB is completely made of 6p* orbitals from Tl^+. Additionally, as the Tl^+ doping concentration increases, the involvement of the orbitals from Cs^+ and Sr^{2+} in the upper CB remains almost similar. Most remarkably, the contribution of the Tl^+-6p* orbitals in the lower CB slightly shifted toward higher energies within the CB.

Similar to the CB, the VB has also been split, which leads to three separate regions: top of the VB, middle and bottom-most. For Cs_4SrI_6:1.52% Tl, the VBM is mostly composed of the same

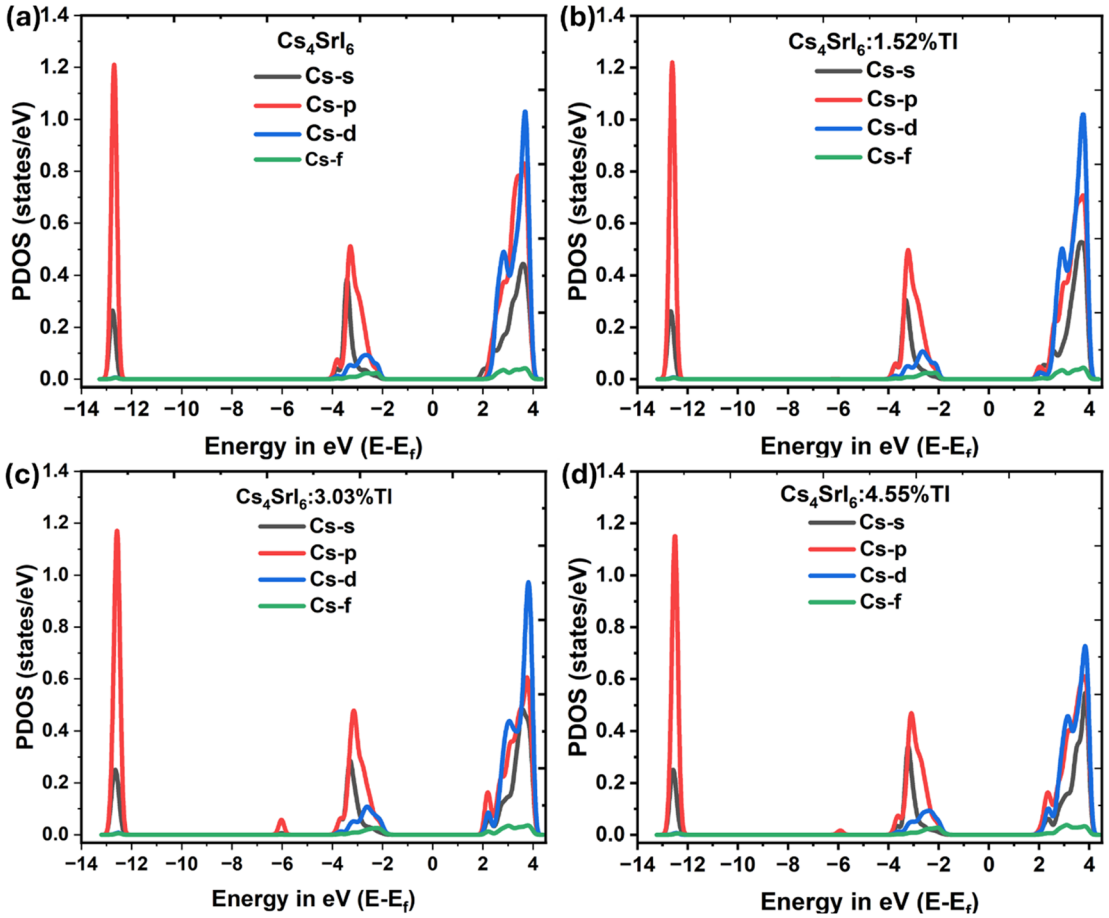

Fig. 7 PDOS plots of the pure and Tl^+-doped Cs_4SrI_6 compounds showing the orbital involvements from Cs^+ ions in (a) pure Cs_4SrI_6, (b) Cs_4SrI_6 doped with 1.52% Tl^+, (c) Cs_4SrI_6 doped with 3.03% Tl^+, and (d) Cs_4SrI_6 doped with 4.55% Tl^+ to electronic states.

orbitals as in pure Cs_4SrI_6, with a minor participation from the Tl^+-6s* orbital. Among all these orbitals, the p atomic orbital from I^- plays the most leading role to form the VB, like pure Cs_4SrI_6. Even though the involvement from other atomic orbitals of Cs^+ (s, p, and d), Sr^{2+} (s and d) and Tl^+ (6p) is in the mid to lower part of the VB top region, the middle VB, positioned at roughly −6 eV, is entirely composed of the 6s atomic orbital from Tl^+ ions. In addition, the core VB (bottom-most), appearing as a narrow energy window from approximately −12.50 eV to −12.80 eV, is mostly formed by involvement from the same atomic orbitals as in the pure Cs_4SrI_6 compound. In addition, the Tl^+-6p orbital also participates slightly to form the core VB.

At low Tl^+ doping concentrations, the Tl^+-6s* orbital shows only a minor involvement near the upper VB formation. However, as the Tl^+ concentration increases, the Tl^+-6s* states become clearly distinguishable and shift to energies above the VBM. Furthermore, the Tl^+-6p* states always appear just below the CBM. As a result, both Tl^+-derived 6s* and 6p* orbitals appeared within the band gap of the host matrix and formed localized impurity states. These mid-gap states arise from the strong hybridization between Tl^+ and halide orbitals and play a crucial role in modifying the electronic structure, charge carrier trapping behavior, and radiative recombination pathways of the material.

Alternatively, this arrangement of Tl^+-derived 6s and 6p states inside the band gap suggests the formation of a two-level activator, which can act as carrier trapping and recombination centers. Such electronic states are expected to strongly influence charge transportation, luminescence efficiency, and energy resolution in radiation detection applications. Actually, the Tl^+-derived 6s and 6p states inside the band gap are known as the antibonding orbital, and they are denoted by Tl^+-6p* and Tl^+-6s*.

Fig. 11 shows the combined PDOS of all constituent atoms, illustrating the relative energy positions of their atomic orbitals. It is observed that the Tl^+-6s* and Tl^+-6p* states appear within the band gap of the host material.

M. H. Du systematically explained that the energetic positions of Tl^+-induced 6s and 6p states in halide scintillators are governed by the strength of hybridization between Tl^+ and halogen ion, and halogen ion and halogen ion, and the ionicity of the host lattice.[37] In general, the Tl^+-6s state lies below the VB, whereas the Tl^+-6p states are positioned above it. Hybridization between Tl^+ and neighboring halogen ions leads to the formation of two antibonding states, namely Tl^+-6p* and Tl^+-6s*, as

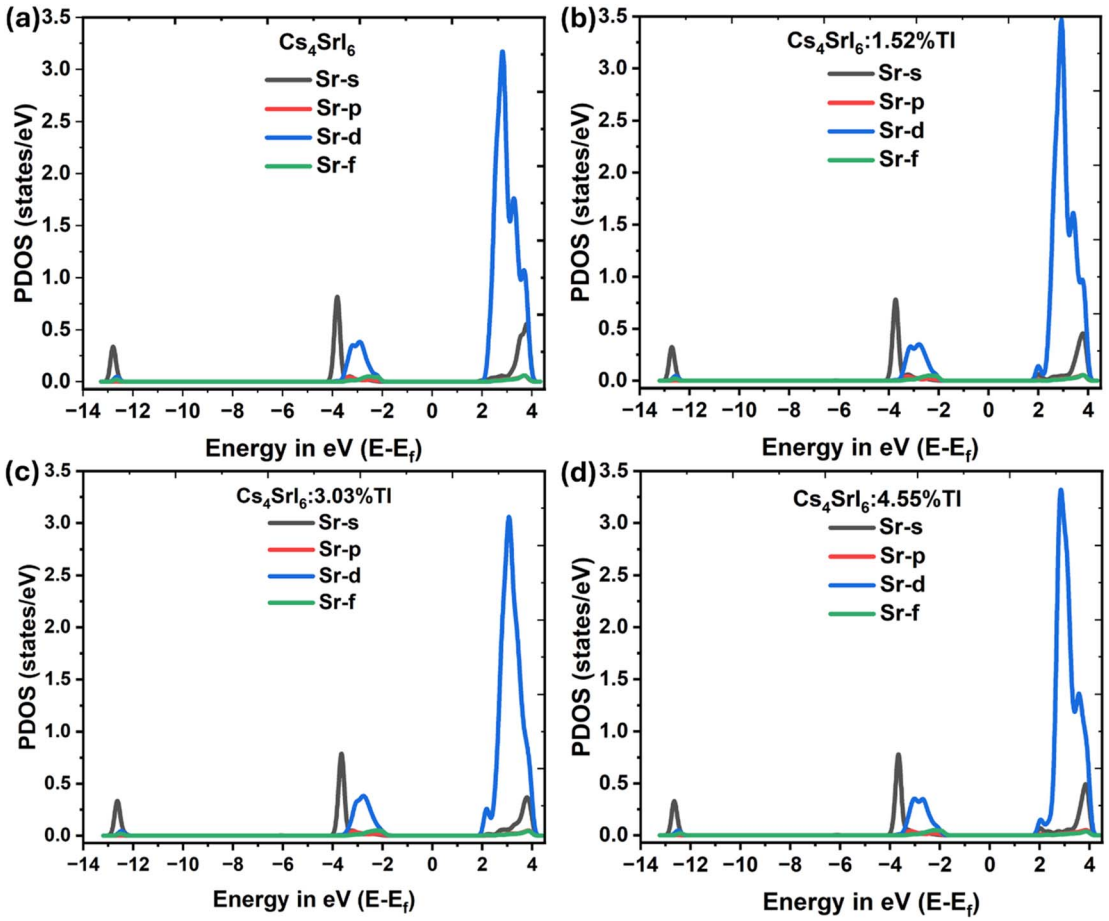

Fig. 8 PDOS plots of the pure and Tl^+-doped Cs_4SrI_6 compounds showing the orbital participation from Sr^{2+} ions in (a) pure Cs_4SrI_6, (b) Cs_4SrI_6 doped with 1.52% Tl^+, (c) Cs_4SrI_6 doped with 3.03% Tl^+, and (d) Cs_4SrI_6 doped with 4.55% Tl^+ to electronic states.

illustrated in Fig. 12. Strong (weak) Tl^+-halogen ion hybridization shifts these Tl^+-6p* and Tl^+-6s* states to higher (lower) energies relative to the VB edges (depicted in Fig. 12).

In addition to Tl^+-halogen ion interactions, halogen ion–halogen ion hybridization within the host lattice also plays a significant role. Strong halogen ion-halogen ion hybridization broadens the VB and lowers the relative positions of the Tl^+-6p* and Tl^+-6s* states with respect to the VBM. Consequently, the relative placement of Tl^+-induced states is governed by the combined effects of Tl^+-halogen ion and halogen ion-halogen ion hybridization.

When strong Tl^+-halogen ion hybridization is coupled with weak halogen ion and halogen ion hybridization, both Tl^+-6p* and Tl^+-6s* levels can reside within the band gap, as depicted in Fig. 12(a). In this configuration, the Tl^+-6s* and Tl^+-6p* states act as hole and electron traps, respectively, enabling radiative recombination. Hence, sometimes Tl^+ is called two-level activator. A similar interaction mechanism is observed in the Tl^+-doped Cs_4SrI_6 structure. In contrast, weak Tl^+-halogen ion hybridization together with strong halogen ion-halogen ion hybridization may result in the situation where only the Tl^+-6p* state lies within the band gap and acts as an electron trap.

However, the studied pure Cs_4SrI_6 compounds initially demonstrate a high band gap. This large intrinsic band gap of the studied compounds gives rise to high electrical resistivity and insulating behavior, thereby dropping the efficiency of charge transportation and ultimately leading to a lower LY than the small-band-gap compound.[38] However, despite the lower LY, this wider band gap offers important advantages, including enhanced ER, lowered afterglow, and better stability under severe radiation exposure.[39,40] Upon Tl^+ doping with different concentrations, the bandgap is decreased, which is anticipated to improve the LY, while remaining an adequately large band gap to prevent adverse effects from thermal quenching. In addition, the dopant incorporation introduces new channels for electron transfer and radiative recombination of charge carriers, which further enhances the scintillation behavior. Moreover, Tl^+ doping can enhance light emission, thereby making the Cs_4SrI_6 structure more effective for radiation detection applications.

3.3 Optical properties

The optical properties of the investigated pure Cs_4SrI_6 and Tl^+-doped Cs_4SrI_6 compounds are discussed in this section. A comprehensive understanding of optical properties including the dielectric function, absorption coefficient, refractive index, *etc.*, is crucial for elucidating the interaction between matter

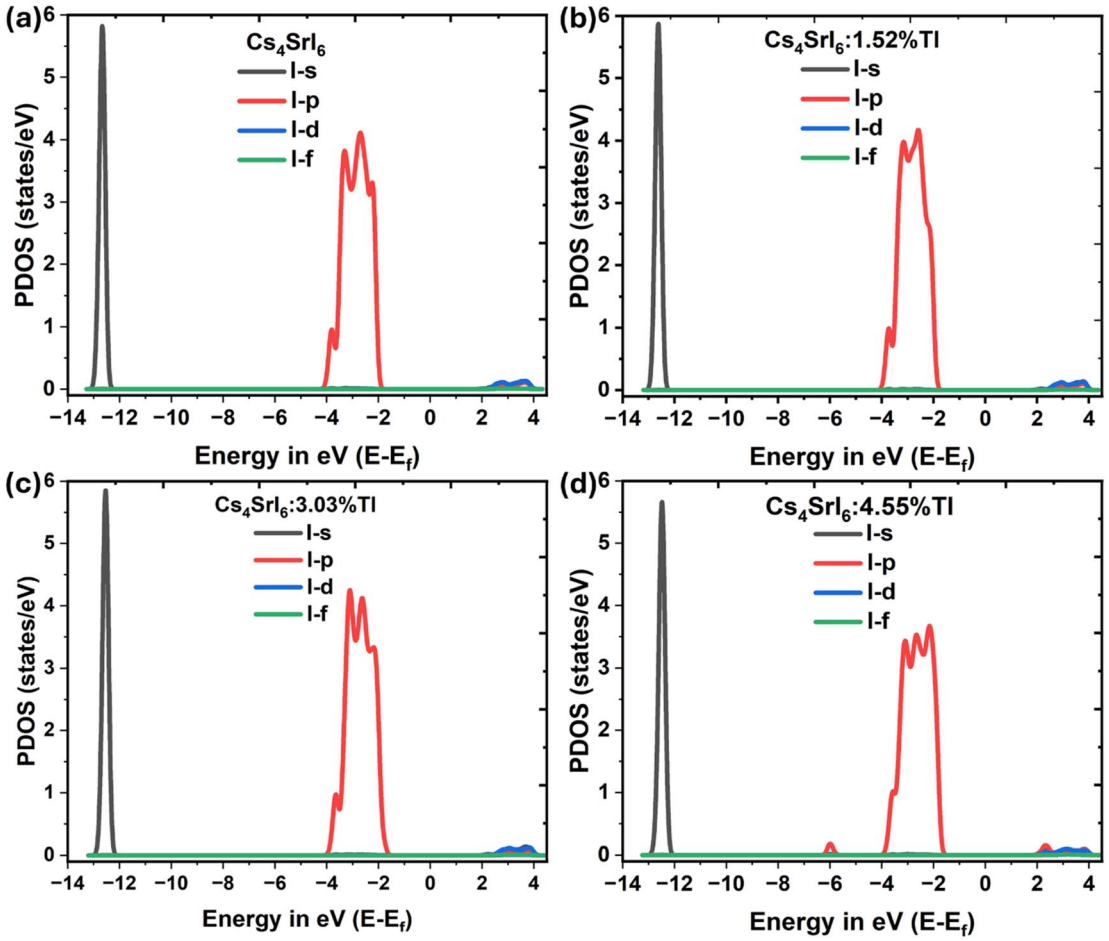

Fig. 9 PDOS plots of the pure and Tl^+-doped Cs_4SrI_6 compounds showing the orbital involvements from I^- atoms in (a) pure Cs_4SrI_6, (b) Cs_4SrI_6 doped with 1.52% Tl^+, (c) Cs_4SrI_6 doped with 3.03% Tl^+, and (d) Cs_4SrI_6 doped with 4.55% Tl^+ to electronic states.

and waves. After effective collisions, electrons from the VB move to the CB, relocating the photon's energy to electrons. In addition, the understanding of electronic transition plays a decisive role in evaluating the scintillation capability of these compounds and predicting their performance in practical device applications. The aforesaid optical features are comprehensively explained in sub-sections 3.3.1 to 3.3.3 and are graphically illustrated in Fig. 13–16 for clarity.

3.3.1 Dielectric function. The real (ε_1) and imaginary (ε_2) components of $\varepsilon(\omega)$ are necessary for understanding the optoelectronic behavior of a compound under irradiation, as they provide insights into its polarization response and optical absorption arising from electronic transitions.[41] Eqn (2)–(4) and Fig. 13 and 14 explain the dispersive component, $\varepsilon_1(\omega)$, and absorptive component, $\varepsilon_2(\omega)$, of the complex $\varepsilon(\omega)$ as a function of photon energy, respectively. The imaginary component of $\varepsilon(\omega)$ links to the electronic transition mechanism under electromagnetic irradiation and is directly associated with optical absorption. In contrast, the real component of $\varepsilon(\omega)$ reflects the non-absorptive interaction of a material with an external electric field, which governs energy storage, transmission, and refractive behavior. Additionally, the real component can be obtained from imaginary components *via* Kramers–Kronig relations. The comprehension of both $\varepsilon_1(\omega)$ and $\varepsilon_2(\omega)$ allows the estimation of main optical features including refractive index and absorption coefficient. Generally, $\varepsilon(\omega)$ is described as follows: $\varepsilon(\omega) = \varepsilon_1(\omega) + i\varepsilon_2(\omega)$.[42] The imaginary component $\varepsilon_2(\omega)$ can be defined by eqn (2) (ref. 43 and 44) as follows:

$$\varepsilon_2(\omega) = \frac{4\pi^2 e^2}{m^2\omega^2}\sum\int \langle i|M|j\rangle^2 f_i(1-f_i)\times\delta\left[E_f - E_i - \omega\right]d^3k, \quad (2)$$

where f_i denotes the Fermi function and M is the momentum operator.

In addition, the real component $\varepsilon_1(\omega)$ is stated by eqn (3) (ref. 45) as follows:

$$\varepsilon_1(\omega) = 1 + \frac{2}{\pi}P\int_0^\infty \frac{\omega'\varepsilon_2(\omega')}{\omega'^2-\omega^2}\mathrm{d}\omega', \quad (3)$$

where P demonstrates the integral's principal value.

The inverse correlation between the material's band gap and the static real component of $\varepsilon(\omega)$ is usually illustrated by using Penn's model (demonstrated in eqn (4))[46] as follows:

$$\varepsilon_1(0) = 1 + \left(\frac{\hbar\omega_p}{E_g}\right)^2, \quad (4)$$

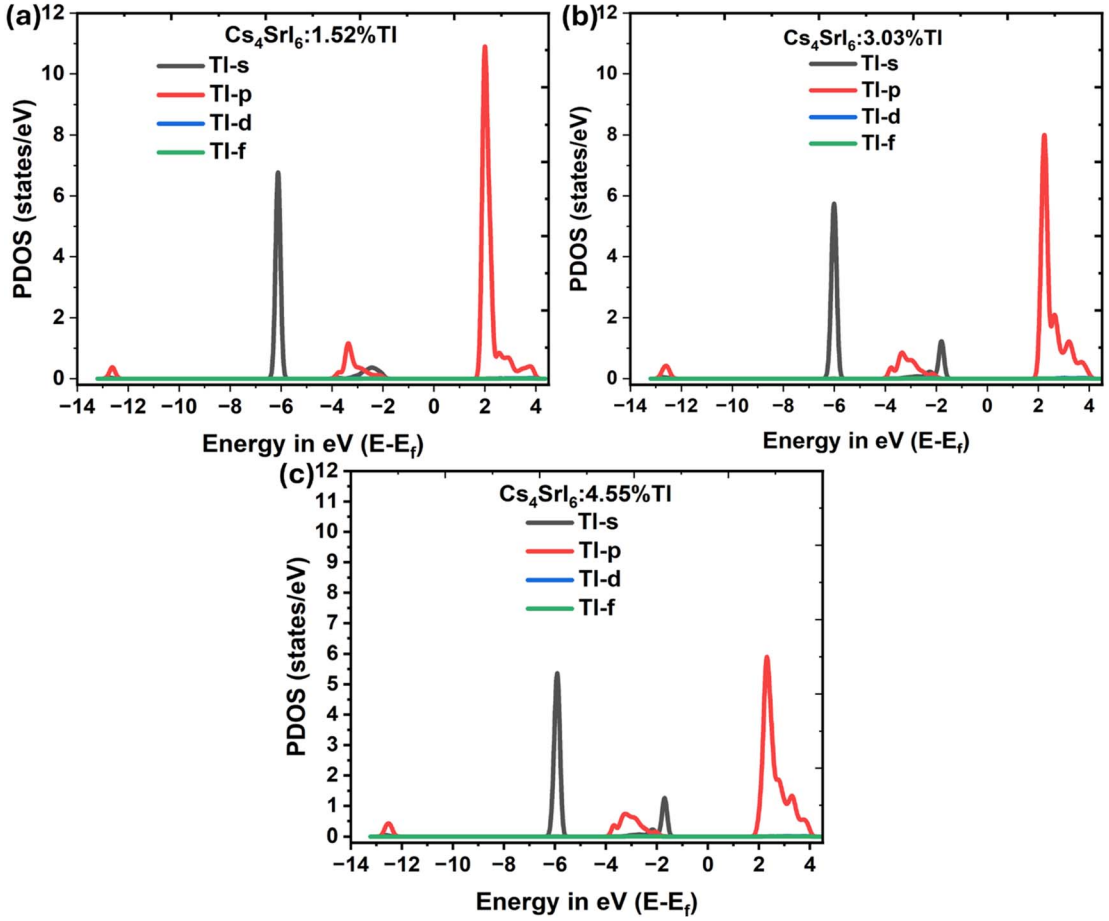

Fig. 10 PDOS plots of the Tl^+-doped Cs_4SrI_6 compounds showing the orbital contributions from Tl^+ ions in (a) Cs_4SrI_6 doped with 1.52% Tl^+, (b) Cs_4SrI_6 doped with 3.03% Tl^+, and (c) Cs_4SrI_6 doped with 4.55% Tl^+ to electronic states. The s and p orbitals from Tl^+ located within the band gap are called antibonding orbitals and are written as 6s* and 6p* in the text.

where ω_p and $\hbar$ signify the plasma frequency and reduced Planck's constant, respectively.

Fig. 13 demonstrates the real component $\varepsilon_1(\omega)$ of $\varepsilon(\omega)$ of pure Cs_4SrI_6 and Tl^+-doped Cs_4SrI_6. The band gaps of the studied materials display a systematic reduction as the Tl^+-dopant concentration increases. In both pure and Tl^+-doped Cs_4SrI_6, the optical band gap is inversely related to the static real dielectric constant, $\varepsilon_1(0)$, which demonstrates qualitative accord with Penn's model. Under the assumptions of the model, a reduction in the band gap leads to an increment in $\varepsilon_1(0)$ owing to augmented polarizability, and this trend is in good agreement with the behavior observed in our investigated compounds.

In Fig. 13, the $\varepsilon_1(\omega)$ value starts at approximately 1.96 at zero photon energy (the static dielectric constant). Upon Tl^+ doping, $\varepsilon_1(0)$ increases gradually. It indicates that Tl^+ introduces highly polarizable $6s^2$ electrons. These electrons enhance local polarization and electronic screening, which are desirable features for efficient scintillation. However, with the increase in photon energy toward 5 eV, the curve rises (normal dispersion) to the peak position, followed by the sharp drop, which is called anomalous dispersion. This type of phenomenon has occurred because the light is vibrating so fast that the electrons can no longer keep up with the field, leading to a "phase shift" in the material's response. Such a behavior indicates that the electrons have lost synchronization with the vibrating light wave, hence collapsing the material's ability to store energy at higher photon energies. Specifically, each investigated compound presented a negative value of $\varepsilon_1(\omega)$ spanning from 6 eV to 8 eV with a peak location at 6.61 eV, 6.58 eV, 6.53 eV and 5.50 eV for pure Cs_4SrI_6, Cs_4SrI_6:1.52%Tl, Cs_4SrI_6:3.03%Tl, and Cs_4SrI_6:4.55%Tl, respectively. Moreover, the negative values for pure Cs_4SrI_6, Cs_4SrI_6:1.52%Tl, Cs_4SrI_6:3.03%Tl and Cs_4SrI_6:4.55%Tl were noted at −1.69, −1.59, −1.55 and −1.48, respectively. Additionally, the negative value of $\varepsilon_1(\omega)$ reveals strong plasmonic behavior, which suggests metallic response in the energy range of 6 eV to 8 eV.

Fig. 14 shows the imaginary part (optical transitions and energy absorption) of the dielectric function of the pure and doped Cs_4SrI_6 sample. This figure shows that $\varepsilon_2(\omega)$ is zero until about 3.7 eV for pure Cs_4SrI_6. More clearly, the absorption edge in $\varepsilon_2(\omega)$ appears at 3.70 eV, which corresponds to an optical band gap of approximately 3.70 eV. It indicates that any light with less energy than 3.70 eV can simply pass through the

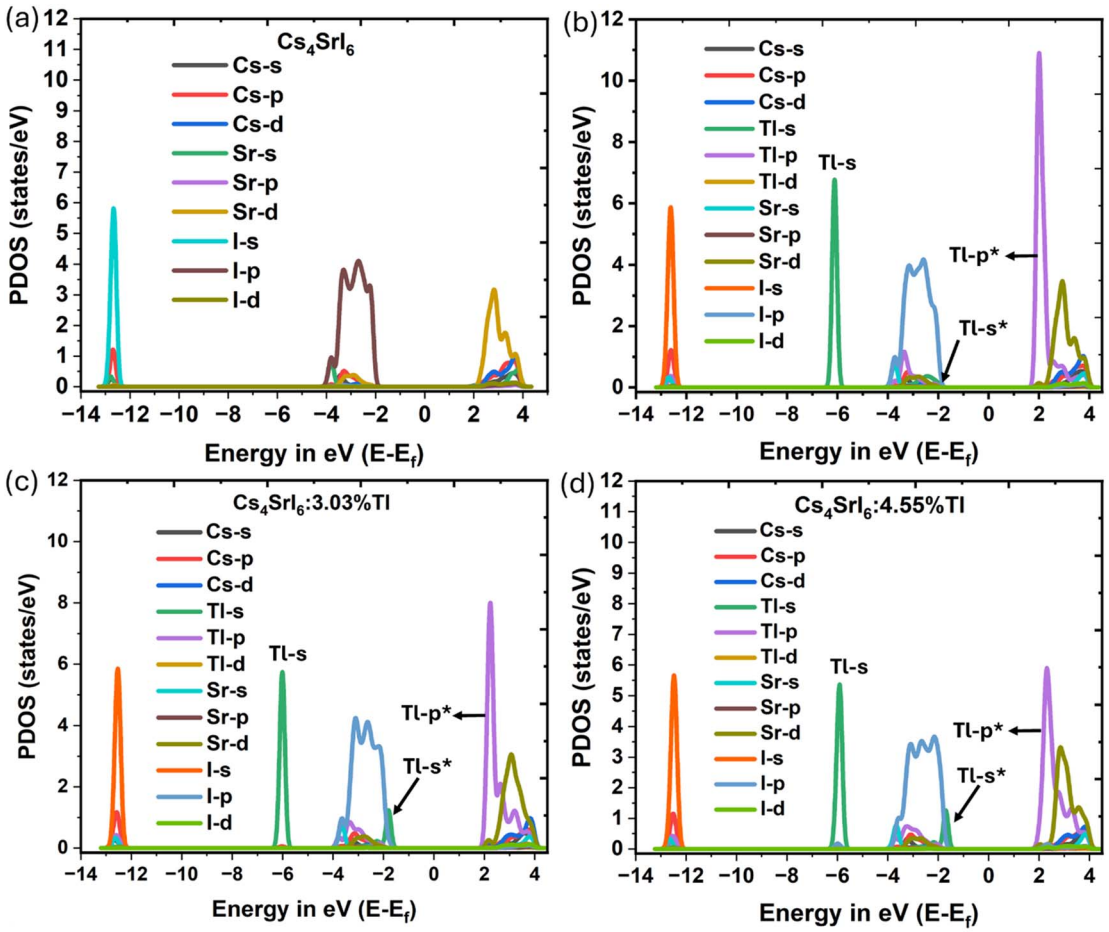

Fig. 11 Combined PDOS plots of the pure and Tl^+-doped Cs_4SrI_6 compounds showing (a) relative atomic orbital involvements from Cs^+, Sr^{2+}, and I^- in pure Cs_4SrI_6. (b) PDOS plots of the 1.52% Tl^+-doped Cs_4SrI_6 showing relative participation from Cs^+, Sr^{2+}, I^-, and Tl^+ ions. (c) PDOS plots of the 3.03% Tl^+-doped Cs_4SrI_6, emphasizing the respective atomic orbital participation from Cs^+, Sr^{2+}, I^-, and Tl^+. (d) PDOS plots of the 4.55% Tl^+-doped Cs_4SrI_6 showing the corresponding atomic orbital involvements from Cs^+, Sr^{2+}, I^-, and Tl^+ to form electronic states. The s and p orbitals from Tl^+ located within the band gap are called antibonding orbitals and denoted as s* and p* in the figure and are written as 6s* and 6p* in the text.

Cs_4SrI_6 crystal, because it does not have enough 'punch' to kick an electron from the valence band to the conduction band. This threshold energy of 3.70 eV also means that the Cs_4SrI_6 material is transparent to visible light, which is a crucial property for a scintillator, so that the light it generates is not reabsorbed by the crystal itself. The band gap extracted from $\varepsilon(\omega)$ may vary from that attained from the electronic band structures owing to differences in underlying theoretical approaches. The $\varepsilon_2(\omega)$ of

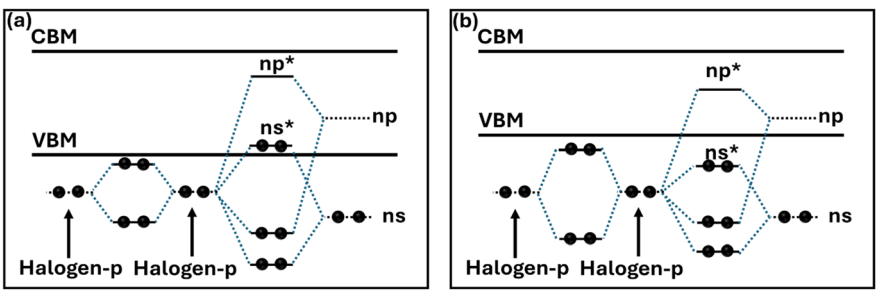

Fig. 12 Schematic of the hybridization between the $6s^2$ (ns^2) state of the Tl^+-activator ion and halogen ions. (a) Strong hybridization between the $6s^2$ state and the halogen ion-p orbitals combined with relatively weak halogen ion-p to halogen ion-p hybridization. (b) Weak hybridization between the $6s^2$ state and the halogen ion-p orbitals accompanied by strong halogen ion-p to halogen ion-p hybridization. This figure is redrawn from ref. 37 with permission from RSC, copyright 2014.

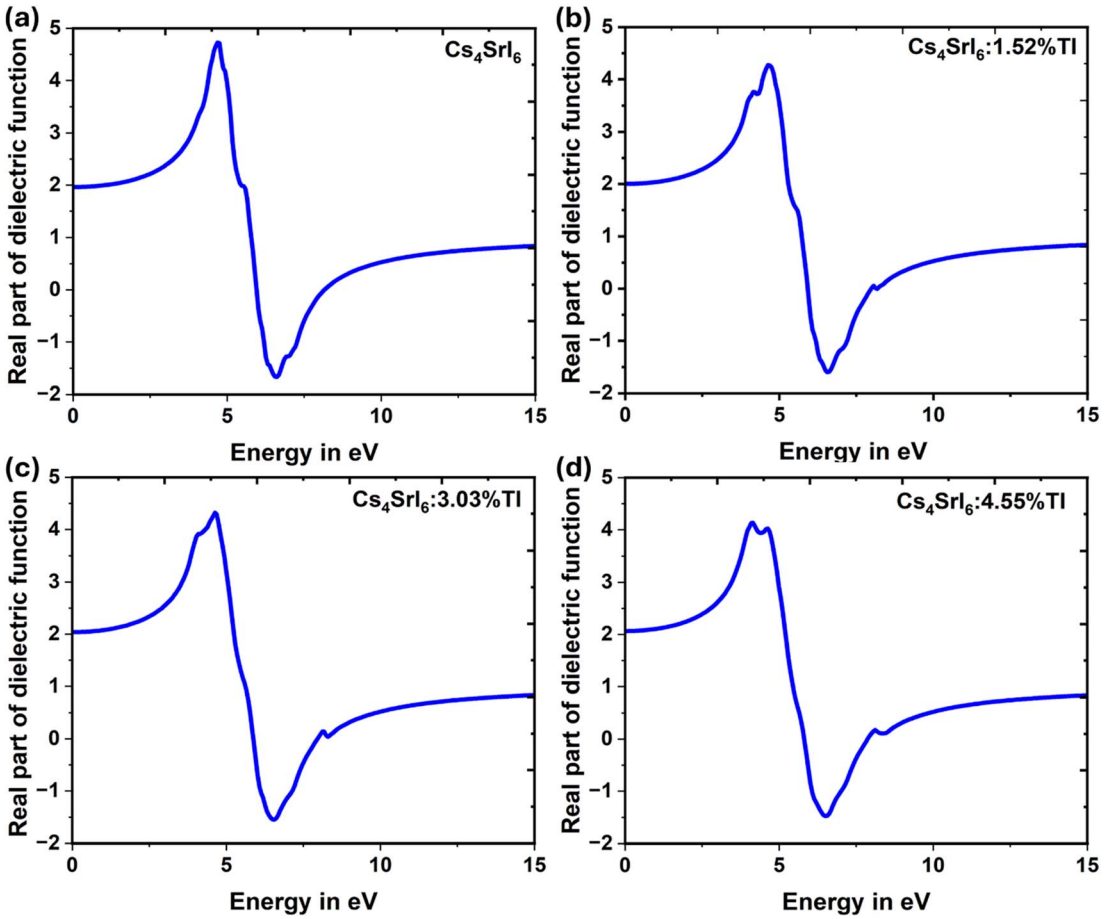

Fig. 13 Dielectric responses of the pure and Tl^+-doped Cs_4SrI_6. Real components of $\varepsilon(\omega)$ for (a) pure, (b) 1.52% Tl^+-doped, (c) 3.03% Tl^+-doped and (d) 4.55% Tl^+-doped Cs_4SrI_6.

$\varepsilon(\omega)$ demonstrates two apparent peaks at 5.14 eV, and 5.86 eV, while the real component $\varepsilon_1(\omega)$ represents corresponding peaks at 4.67 eV and 6.58 eV, respectively. An investigation of PDOS reveals that the VB is mainly made of I^--p states, while the CB is primarily composed of Sr^{2+}-d states with minor participation from Cs^+ orbitals. Consequently, the distinct peaks in $\varepsilon_2(\omega)$ at 5.14 eV and 5.86 eV, and the corresponding peaks in $\varepsilon_1(\omega)$ at 4.67 eV and 6.58 eV, can be ascribed mainly to interband electronic transitions from the I^--p states of the VB to the Sr^{2+}-d states of the CB, occurring in different energy ranges of the band structure.

Upon 1.52% Tl^+ doping in pure Cs_4SrI_6, the beginning of the absorption edge in $\varepsilon_2(\omega)$ moves to 3.44 eV, which reveals the decrease in band gap. The $\varepsilon_2(\omega)$ graph presents four visible peaks at 4.26 eV, 5.19 eV, 5.90 eV, and 8.09 eV, whereas the $\varepsilon_1(\omega)$ confirms corresponding features at 4.15 eV, 4.63 eV, 6.58 eV and 8.05 eV, respectively. After Tl^+ doping in the position of Cs^+, two extra noticeable characters (bumps) occur in the $\varepsilon_2(\omega)$ ($\varepsilon_1(\omega)$) spectrum at 4.26 eV (4.15 eV) and 8.09 eV (8.05 eV). These features are attributed to electronic transitions associated with the dopant-induced states. The observed peaks at 4.26 eV and 4.15 eV appeared due to possible electron transfer from the Tl^+-6s* (upper VB) states to the Tl^+-6p* state. In addition, the peaks at 5.19 eV and 4.63 eV originate due to electron transfer from the I^--p orbital to the Sr^{2+}-d orbital. Moreover, the peaks at 5.90 eV and 6.58 eV may arise owing to the same electron transfer process from the I^--p orbital to the Sr^{2+}-d orbital. Finally, the peaks at 8.09 eV and 8.05 eV may be related to electron transfer from the core Tl^+-6s orbital to the Tl^+-6p* orbital in the conduction band, as it appears after doping and its strength is very low.

At a higher Tl^+-dopant concentration of 3.03%, the commencement of the absorption edge in $\varepsilon_2(\omega)$is perceived at 3.32 eV. in addition, the first peak (4.26 eV) observed for 1.52% doping is shifted toward the second peak due to enhanced hybridization of Tl^+-induced electronic states at this higher dopant concentration. As a result, the first peaks almost disappear into the second peak, and hence, the intensity of the second peak is increased. Consequently, $\varepsilon_2(\omega)$ displays three distinguishable peaks at 5.14 eV, 5.79 eV and 8.25 eV, while $\varepsilon_1(\omega)$ reveals four distinct peaks at 4.08 eV, 4.63 eV, 6.54 eV and 8.09 eV. From the $\varepsilon_1(\omega)$ spectrum, enhanced electronic transitions are observed at 4.08 eV and 8.09 eV. These features can be attributed to transitions involving Tl^+-derived states, specifically from the upper Tl^+-6s* states (above VB) and deeper (core-like) Tl^+-6s states to the lower-lying Tl^+-6p* states within the conduction band.

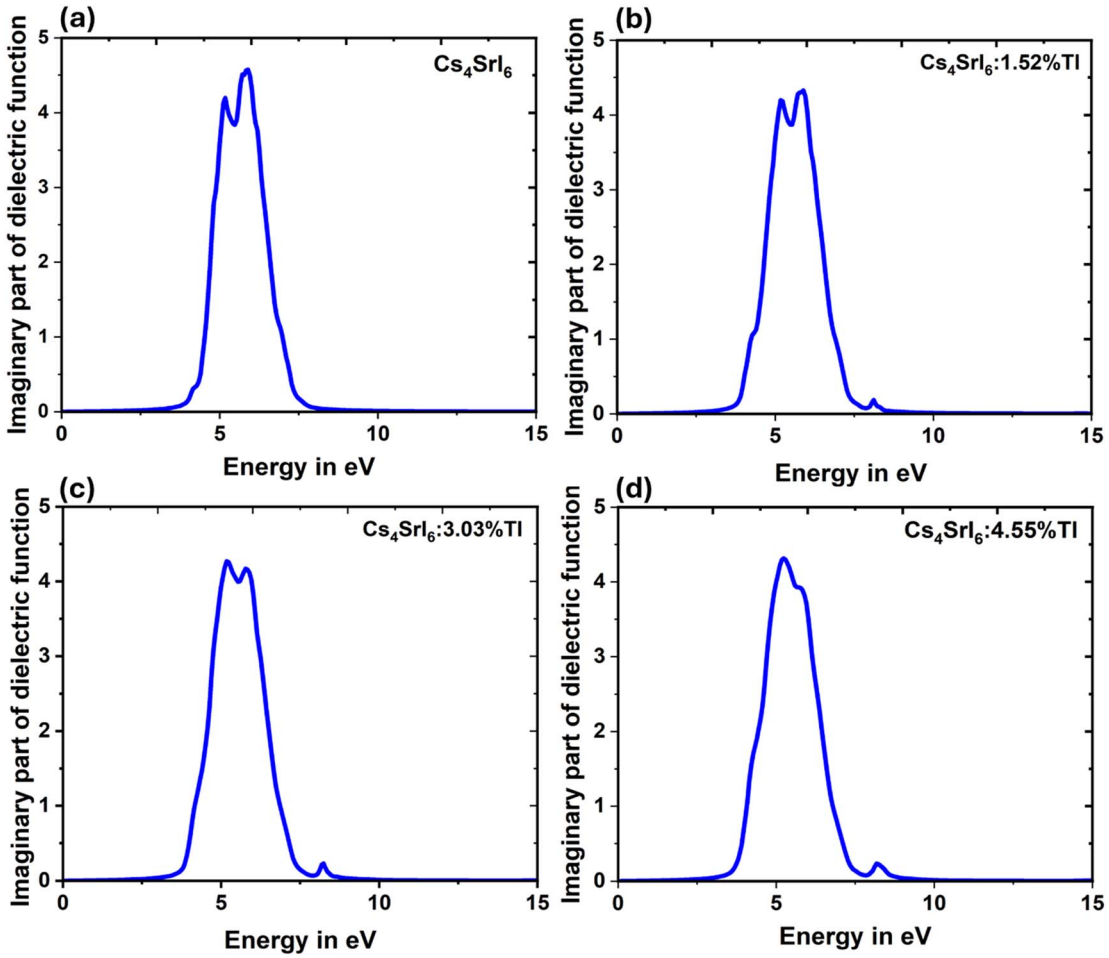

Fig. 14 Dielectric responses of the pure and Tl^+-doped Cs_4SrI_6. Imaginary components of $\varepsilon(\omega)$ for (a) pure, (b) 1.52% Tl^+-doped, (c) 3.03% Tl^+-doped and (d) 4.55% Tl^+-doped Cs_4SrI_6.

In addition, at a higher Tl^+-dopant concentration of 4.55%, the beginning of the absorption edge in $\varepsilon_2(\omega)$ is noted at 3.21 eV. However, the Tl^+-6s* and Tl^+-6p* states are positioned within the band gap, similar to the behavior observed in the previously discussed structures. Consequently, electronic transitions from the deeper (core-like) Tl^+-6s states and the upper Tl^+-6s* states located above the valence band to the Tl^+-6p* states are relatively enhanced compared with the lower-doped structures. The progressively enhanced intensity of the Tl^+-related peaks confirms the dominant role of dopant-derived states in governing the dielectric and optical behavior of the doped system.

3.3.2 Refractive index. The refractive index, $n(\omega)$, plays a critical role in explaining the optoelectronic response of a material by describing how light is scattered during interaction.[47] It impacts the dispersion of the electromagnetic radiation and determines the effective speed of light inside the materials. In addition, it can be evaluated by employing eqn (5) (ref. 48) as follows:

$$n(\omega) = \left[\frac{\varepsilon_1(\omega)}{2} + \frac{\sqrt{\varepsilon_1^2(\omega) + \varepsilon_2^2(\omega)}}{2}\right]^{\frac{1}{2}} \quad (5)$$

This quantity is also allied with the real section of $\varepsilon(\omega)$ as well as extinction coefficient, as described by eqn (6) and graphically represented by Fig. 15 for pure and doped Cs_4SrI_6 compounds as follows:

$$n^2(\omega) - k^2(\omega) = \varepsilon_1(\omega) \quad (6)$$

Furthermore, the essential relationship between static $n(\omega)$ and the static dielectric constant is explained by the formula $n^2(0) = \varepsilon_1(0)$. The values of $n(0)$ for the four investigated compounds were perceived at 1.40 for pure Cs_4SrI_6, 1.42 for Cs_4SrI_6:1.52%Tl, 1.43 for Cs_4SrI_6:3.03%Tl and 1.44 for Cs_4SrI_6:4.55%Tl. Throughout the visible range of light, spanning from 1.55 eV (780 nm) to 3.44 eV (360 nm), the $n(\omega)$ displayed deviation. Particularly, for pure Cs_4SrI_6, it varied from 1.43 to 1.61, while for Cs_4SrI_6:1.52%Tl and Cs_4SrI_6:3.03%Tl, the values $n(\omega)$ spanned from 1.45 to 1.66 and 1.46 to 1.68, respectively. For the final Tl^+-dopant concentration at 4.55%, the variation was 1.47 to 1.73.

When Tl^+ acts as a two-level activator, it emits at a characteristic wavelength.[20] For example, the well-known NaI:Tl scintillator exhibits a characteristic emission peak at ~412 nm

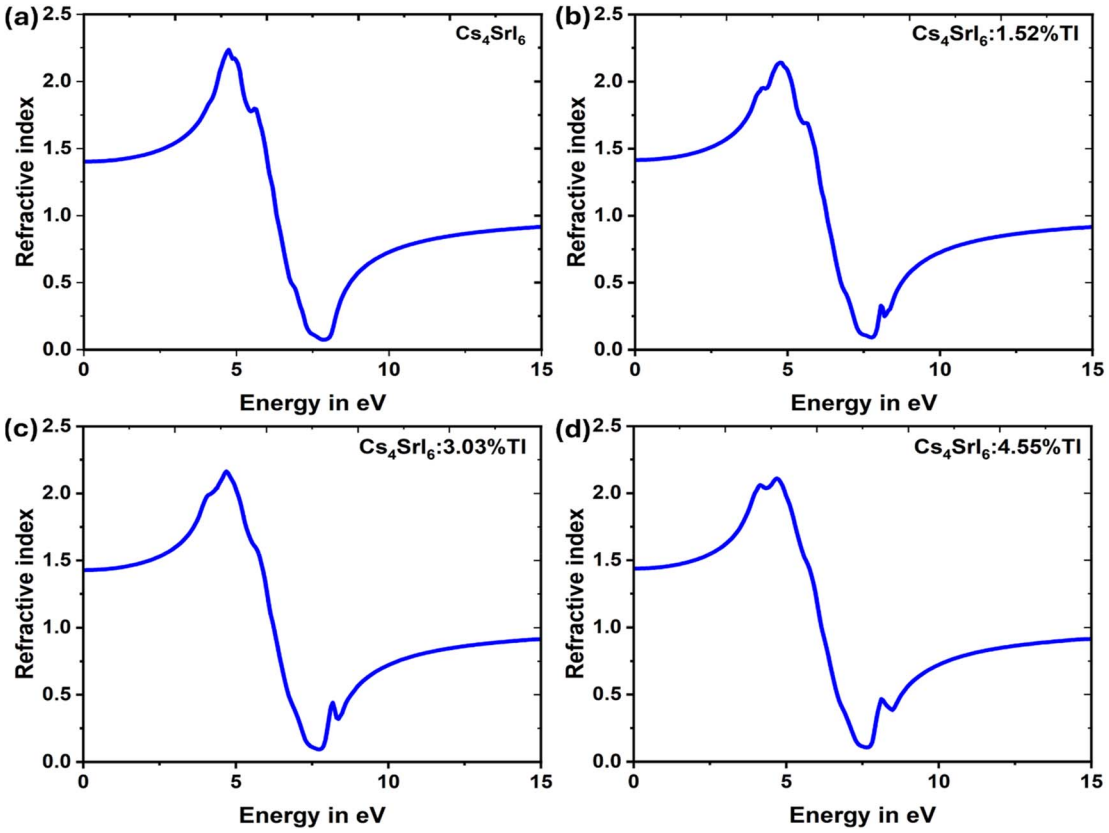

Fig. 15 Refractive index, $n(\omega)$ responses of (a) pure, (b) 1.52% Tl^+-doped, (c) 3.03% Tl^+-doped and (d) 4.55% Tl^+-doped Cs_4SrI_6.

(≈3.01 eV), originating from electronic transitions between Tl^+-6p* excited states and Tl^+-6s* states.[20] In the present studied structures, Tl^+ is also found to operate as a two-level activator, indicating a similar radiative recombination mechanism (Tl^+-6p* state to Tl^+-6s* state). The corresponding refractive indices of the Tl^+-doped studied structures at this emission wavelength are approximately 1.57, 1.60, and 1.62. These values are not sufficiently high to cause a significant refractive-index mismatch at the interface between the scintillator and the photomultiplier tube (PMT) glass. Any remaining mismatch can be effectively minimized by using optical coupling grease, which creates a refractive-index gradient at the interface, and thus, enhances light transmission and improves the scintillation light collection efficiency by the PMT.

The above-discussion emphasizes that the refractive index compatibility between the scintillator material, optical coupling medium, and PMT glass plays a crucial role in improving light transmission and photon collection efficiency in scintillation-based detection systems. When photons are produced through the scintillation process, they are released isotropically from the source, covering a full 4π solid angle and their reaching out at the PMT can be affected by the variance of $n(\omega)$ among the compounds, optical coupling grease, and window glass of PMT. Moreover, as predicted by Snell's law, light can escape the compound and reach at PMT only when their incidence angle at the interface is smaller than the critical angle. However, photons with incidence angles exceeding the critical angle are confined within the material because of total internal reflection. Therefore, a substantial mismatch of $n(\omega)$ can launch total internal reflection. As a result, light is trapped inside the scintillator compound and reduced the availability for detection.

Therefore, a controlled refractive index is necessary for a material to be used as a high-efficiency scintillator. Fig. 15 shows that Tl^+-doping (1.52% to 4.55%) only slightly modifies $n(\omega)$ in the range of ~1.43 to 1.47 and 1.61 to 1.73 for lower and upper ranges of visible light, respectively, meaning that the light-extraction efficiency remains stable even if more dopant concentration is added.

3.3.3 Absorption coefficient. The absorption spectrum plays a critical role in defining the scintillation performance of substances. The absorption coefficient ($\alpha(\omega)$) measures the attenuation of light per unit length of material *via* interaction as it propagates through the substances. $\alpha(\omega)$ can be determined by using eqn (7) (ref. 49) as follows:

$$\alpha(\omega) = \frac{\sqrt{2}\omega}{c}\left[\sqrt{\varepsilon_1{}^2(\omega) + \varepsilon_2{}^2(\omega)} - \varepsilon_1(\omega)\right]^{\frac{1}{2}} \quad (7)$$

For the investigated compounds of pure Cs_4SrI_6, Cs_4SrI_6:1.52%Tl, Cs_4SrI_6:3.03%Tl and Cs_4SrI_6:4.55%Tl, $\alpha(\omega)$ was acquired from the imaginary and real components of $\varepsilon(\omega)$ ($\varepsilon_2(\omega)$ and $\varepsilon_1(\omega)$) as a function of photon energy. The absorption behavior of a substance can be interpreted using this $\alpha(\omega)$,

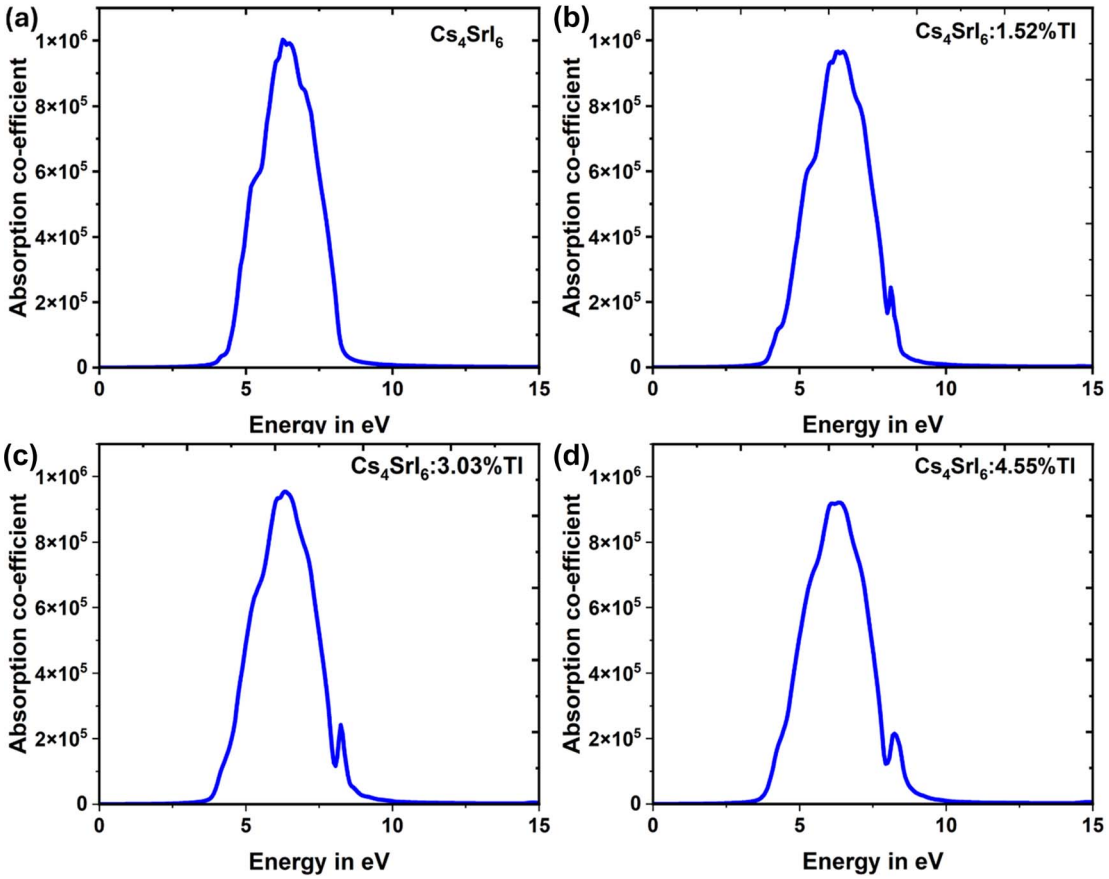

Fig. 16 Absorption coefficient responses of (a) pure, (b) 1.52% Tl^+-doped, (c) 3.03% Tl^+-doped and (d) 4.55% Tl^+-doped Cs_4SrI_6.

which is directly linked with the imaginary component of $\varepsilon(\omega)$ and often fulfills an equivalent purpose. Particularly, $\varepsilon_2(\omega)$ is exactly proportional to the absorption spectrum, which is depicted in associated Fig. 16. The zero values of $\alpha(\omega)$ intimately coincide with those of the imaginary part of $\varepsilon(\omega)$, with minor discrepancies arising from the self-consistent approximations inherent in the DFT framework. In spite of these variations, the overall behavior remains consistent. For all investigated compounds, pure Cs_4SrI_6, Cs_4SrI_6:1.52%Tl, Cs_4SrI_6:3.03%Tl and Cs_4SrI_6:4.55%Tl, optical response was not noted below 3.82 eV, 3.7 eV, 3.63 eV and 3.52 eV, respectively, which recommends that the band gap is around these energies. Clear absorptions were perceived at ranges of 3.82 eV to 9.44 eV, 3.7 eV to 9.57 eV, 3.63 eV to 9.84 eV and 3.52 eV to 9.88 eV for pure Cs_4SrI_6, Cs_4SrI_6:1.52%Tl, Cs_4SrI6:3.03%Tl and Cs_4SrI6:4.55%Tl, respectively. Beyond this range, each compound displays transparency. This implies that the absorption coefficient in the range of visible light, around 1.55 eV (780 nm) to 3.44 eV (360 nm), is insignificant. Such optical transparency in the visible area is a required feature for scintillating substances, as it reduces the reabsorption of released scintillation photons, and thus, enhances the light transport efficiency and overall performance of detectors.

In addition, since the optical properties are derived from the real and imaginary components of $\varepsilon(\omega)$, the observed optical transitions originate from the same electronic orbitals that were discussed in the imaginary part of $\varepsilon(\omega)$. Absorption spectra also confirm that Tl^+ doping introduces two additional optical transition pathways. More specifically, the Tl^+-6s* and Tl^+-6p* states are positioned within the band gap and Tl^+-6s is positioned deeper in the core valence band. Consequently, electronic transitions from the deeper (core-like) Tl^+-6s states as well as from the upper Tl^+-6s* states located above the VB to the Tl^+-6p* states are relatively enhanced compared with the lower-doped structures. The progressive increase in the intensity of the Tl^+-related peaks confirms the dominant role of dopant-derived states in governing the dielectric response and optical behavior of the doped system.

4 Light yield and cross band luminescence

In inorganic scintillators, appropriate luminescence at ambient temperature is commonly achieved by employing activators. Certain activators launch two discrete energy levels within the band gap of host materials, with each level selectively capturing one type of charge carrier.[50–52] However, with a reduction in the band gap, this mechanism may lose effectiveness, since a smaller gap cannot accommodate two distinct energy states within the band gap, and the accompanying increase in covalency inhibits carrier self-trapping.[53] As reported in the existing literature, beyond excitonic and defect-assisted emission,

scintillation in Tl^+-doped scintillators proceeds through multiple mechanisms, all of which contribute substantially to the overall LY. Since Tl^+ acts as a two-level activator in the studied Cs_4SrI_6 structure, analogous to its role in conventional NaI:Tl scintillators, the scintillation emission mechanism can be described as follows. The first procedure is rapid Tl^+-activation that originates either by means of direct energy absorption from incident radiation or *via* sequential electron and hole capture at the Tl^+ activator, or by apprehending an STE at the Tl^+ activator to be excited $(Tl^+)^*$.[20,53,54] In this mechanism, an electron of Tl^+ ($6s^2 \approx Tl^+$-6s*) is moved to the excited state ($6s^16p^1 \approx Tl^+$-6p*). Subsequently, luminescence is produced through radiative de-excitation of the excited Tl^+ center (*i.e.*, $6s^16p^1(Tl^+$-6p*) $\rightarrow 6s^2$ (Tl^+-6s*)). The second process is relatively slow and is initiated when a Tl^+ ion is changed to Tl^0 through rapid electron capture. This is followed by the immediate self-trapping of free holes in the VB, forming STHs that subsequently diffuse toward and are trapped within the Tl^0 centers. Consequently, an excited Tl^+ state, (Tl^+)*, is produced. Therefore, radiative de-excitation of (Tl^+)* again leads to light emissions.[20,54–56] These two mechanisms together constitute the fast decay component observed in NaI:Tl scintillators. The third mechanism is relatively delayed and begins with the rapid confinement of an electron by a Tl^+ center, and then it is transformed to Tl^0. This is followed by the diffusion of STHs, which are trapped by Tl^+ centers to produce Tl^{2+}. At later times, delayed electrons are released from Tl^0 traps and subsequently confined by Tl^{2+} centers, resulting in the formation of (Tl^+)*. This state undergoes radiative de-excitation by emitting the subsequent luminescence.[20] In our investigation, the PDOS analysis revealed that the Tl^+-6p* and Tl^+-6s* orbitals lie inside band gaps similar to the NaI:Tl scintillator.[20] Therefore, the studied compounds (Cs_4SrI_6:Tl) are anticipated to demonstrate radiative recombination mechanisms comparable to those observed in NaI:Tl scintillators. Moreover, although excitons can involve light emissions, their relatively weak binding energies often limit their stability at ambient temperature.[34] In investigated perovskites (Tl^+-doped Cs_4SrI_6), STEs or STHs can form easily and remain stable due to the flat nature of the valence and conduction edges. These localized STEs and STHs typically enhance radiative recombination and light emission. However, the beneficial effects of doping are only achieved within an optimal concentration range. When the dopant concentration becomes excessively high, the material experiences concentration quenching, a well-known phenomenon in which the proximity of activator ions facilitates non-radiative energy transfer pathways. These pathways compete with radiative recombination and ultimately lead to a reduction in radiant efficiency and a noticeable decrease in light output. Therefore, maintaining an appropriate balance in Tl^+ concentration is essential for maximizing the scintillation efficiency.

In addition to its impact on luminescence, thallium ion doping modifies the electronic band structure of Cs_4SrI_6. The changes in the band structure, particularly in the band gap, directly influence the optical absorption, emission efficiency, and charge-carrier dynamics within the material. To quantify these effects, the band gap E_g of the undoped and doped compounds was extracted from the electronic band structure. For Cs_4SrI_6:Tl, depending on the role of Tl^+ in the host material (whether it works as a two-level or single-level activator), the dominant emission occurs. In general, if it works as a single-level activator, it may emit radiation ranging from 500 nm to 600 nm.[57,58] However, a prominent emission peak usually occurred at around 550 nm.[58,59] However, if it works as a two-level activator, it emits radiation ranging from 410 nm to 420 nm.[20,60,61] Since Tl^+ acts as a two-level activator in our structure, the emission peak is expected to occur at around the mentioned ranges. However, the emission energy of Tl^+ ($6s^16p^1 \rightarrow 6s^2$ transition) is strongly dependent on the host matrix. To estimate the maximum possible radiant quantum efficiency of the phosphor, the peak energy difference between the Tl^+-6p* and Tl^+-6s* states was considered as emitted energy, as the radiative transition is expected to occur between these two states. Under ideal conditions, the intrinsic luminescence quantum efficiency (Q) and the energy-transfer efficiency (S) are considered to be equal to unity. The radiant quantum efficiency (QE) can be expressed by eqn (8) as follows[62]:

$$\eta = \frac{h\nu_e}{E} S \cdot Q \tag{8}$$

This expression provides a theoretical estimation of the energy conversion capability of the phosphor, relating the emitted photon energy to the electronic band-gap energy of the host material. In self-activated scintillators, holes and electrons can form excitons bound to native atoms or induce local lattice distortions, leading to the formation of STEs, which subsequently undergo radiative recombination. In these instances, S needs to be redefined as the possibility of an electron–hole pair forming a bound exciton, or an STE, while Q corresponds to the quantum efficiency of an exciton. $E = \beta E_g$ act for the necessary energy to produce an electron–hole pair, where β reveals that only a fragment of radiation energy stimulates electron–hole pairs. Therefore, the remaining energy is dissipated through nonradiative channels, primarily as lattice vibrations (phonons). In addition, the parameter β is generally larger in covalent materials ($\beta \approx 3-4$) than in ionic materials ($\beta \approx 1.5$–2), owing to more efficient energy transfer to phonons in covalent substances.[48,63] Recently, based on the experimental investigations of various scintillators and the application of a practical empirical formula, the value of β has been estimated to be 2.5.[64]

To understand how efficiently the absorbed energy is converted into emitted light, the radiant quantum efficiency was calculated using the expected emission energy of the Tl^+ activator in the investigated doped structures. The calculated QE values are 39.52%, 41.41%, and 43.70% for Cs_4SrI_6 doped with 1.52%, 3.03%, and 4.55% Tl^+, respectively. The undoped Cs_4SrI_6 sample was excluded from the QE analysis due to the unknown emission peak energy. Although the radiant quantum efficiency increases with the increase in Tl^+ doping concentration under ideal conditions, in practical systems, higher dopant concentrations may lead to concentration quenching, which can reduce the overall energy conversion efficiency.

Furthermore, the variation in light output with the thallium concentration was examined to understand the interplay between the dopant level, band-gap modification, and scintillation yield. The light output of Cs_4SrI_6 is inversely proportional to the band gap, meaning that as the band gap decreases, typically with the increasing dopant concentration, the material can more efficiently convert absorbed energy into optical emission. However, this enhancement does not continue indefinitely. At higher Tl^+ concentrations, the light output tends to plateau, indicating a saturation behavior beyond which additional doping no longer improves the performance and may even degrade it due to quenching effects. This trend emphasizes the importance of optimizing the dopant concentration not only for maximizing LY but also for preserving the intrinsic scintillation mechanisms within the material.

The light yield, upon irradiation to high energy, is a key parameter for evaluating the scintillator performance. Additionally, an enhanced LY offers greater resolution of a scintillator. The LY, usually calculated as the number of photons per MeV of radiation energy, is stated as eqn (9) as follows:[62,65,66]

$$\mathrm{LY} = \frac{SQ}{\beta E_g} \times 10^6 \text{photons per MeV}. \quad (9)$$

The relatively small band gaps of perovskite materials, compared with traditional scintillators (NaI: 5.9 eV, CsI: 6.4 eV and BGO: 5 eV), suggest a higher theoretical LY of approximately 129 000–250 000 photons per MeV. Despite this advantage, perovskite materials have not yet achieved comparable levels of LY.[67,68] Utilizing ideal settings, LY is estimated by assuming β for 2.5, and Q and S for 1. Therefore, the pure Cs_4SrI_6 structure can attain a superior LY of 97 324 photons per MeV, whereas the compound Cs_4SrI_6 doped with 1.52% 3.03% and 4.55% Tl^+ can attain LY of 100 503 photons per MeV, 102 564 photons per MeV and 108 401 photons per MeV, respectively.

In addition to radiative recombination related to Tl^+-mediated emission and excitonic emission, cross-luminescence, also recognized as core-valence luminescence or Auger-free luminescence, can participate in light emission. This luminescence is initiated from the radiative recombination of a VB electron with a hole in the highest core band. This event is mainly perceived in halide scintillators containing heavier alkali metal halides or alkaline earth metal halides or a stoichiometric mixture of them.[69–73] Particularly, halide compounds including KI, RbI, CsI, BaI_2 and halide perovskites display cross-luminescence. A detailed light emission procedure is portrayed in Fig. 1. In contrast to traditional luminescence mechanisms, this cross-luminescence mechanism proceeds *via* an interionic transition, in which an electron from the anion-derived VB directly recombines with a cation core hole.[72] Such a transition becomes possible because the VB, mainly derived from anion states, is located energetically above the highest core VB associated with cation states. As a result, radiative recombination can occur directly between a VB electron and a core hole, which produces photon emissions with an exceptionally fast decay time, since the competing nonradiative Auger process is effectively suppressed.[74] Due to this unique emission mechanism, compounds that display cross-luminescence are especially valuable for fast-timing radiation detection applications.

The substances that exhibit cross-luminescence are categorized as L-type scintillators and differentiated by $E_g > E_{vc}$.[75,76] Conversely, the substances present Auger luminescence-labelled A-type scintillators, and are distinguished by $E_g < E_{vc}$. Moreover, the materials described by $E_g > E_{vc} - \Delta E_v$ are labelled as AL-type.[76] The distinctive band orientation in AL-type substances allows fast scintillation, which makes them remarkably capable for fast-response applications.

Our pure Cs_4SrI_6 demonstrates the correlation $E_g < E_{vc}$, representing that it works as an A-type device. Owing to the higher photon energy from cross-luminescence in comparison with conventional emissions, this photon may be capable of exciting the electrons from the VB. This process actually prolongs the apparent decay time of emitted photons, reduces the resolution of the scintillator and increases non-proportionally.[77] Upon Tl^+ doping, the cross-band emission channels are altered such that it behaves as an AL-type scintillator as it now obeys the criterion $E_g > E_{vc1} - \Delta E_v$. Under this condition, luminescence generated through cross-band transitions is not reabsorbed by VB electrons, thereby reducing self-absorption losses. This process can be described by the Auger-free luminescence process. Particularly, this cross-band transfer of electrons can occur from the I^--p derived states or other orbitals (which contribute to the VB) to the Tl^+-6s state located deep within the core valence region. This explanation is corroborated by our assessed optical properties, which demonstrate that electronic transitions from deeper Tl^+-6s states to Tl^+-6p* states become increasingly pronounced with higher Tl^+-dopant concentrations. To compensate for the hole generation in the Tl^+-6s state (deeper), an electron from the I^--p-controlled VB undergoes a fast radiative transition, which provides a fast cross-luminescence.

Finally, the main achievement of this work is the identification and clarification of the role of Tl^+ in the emission mechanism, which is expected to operate effectively as a two-level activator in Cs_4SrI_6. However, the emitted energy may vary depending on the relative positions of the Tl^+-6p* and Tl^+-6s* states. Achieving high scintillation performance, including high light yield and radiant quantum efficiency, depends on several factors such as crystal quality, optimal activator concentration, uniform activator distribution, efficient transfer of charge carriers to the activator, phase purity, and the presence of defects. If these factors are properly managed, the experimentally measured performance may approach the predicted theoretical values. In this study, we assumed ideal conditions where the intrinsic luminescence quantum efficiency and the energy-transfer efficiency are both equal to unity. However, such ideal conditions are challenging to be realized experimentally, and therefore, the actual experimental performance is expected to be lower than theoretical predictions.

5 Conclusion

In this research study, DFT calculations were carried out to understand the role of Tl^+ in the scintillation application of

Cs_4SrI_6 and the scintillating behaviors of pure Cs_4SrI_6 and Cs_4SrI_6:Tl through exploring the electronic and optical properties. The exploration of band structures discovered that the Tl^+ dopant transforms the band gap of Cs_4SrI_6 by reducing its direct band gap from 4.11 eV for pure Cs_4SrI_6 to 3.69 eV for Cs_4SrI_6:4.55%Tl. This electronic modification stems from dopant-induced band splitting driven by electronegativity differences among the constituent elements. More specifically, the strong interaction of the Tl^+-halogen ion couple with the weak interaction of halogen ion-halogen ion leads to the formation of two antibonding states, namely Tl^+-6s* and Tl^+-6p*. As a result, the Tl^+-6p* orbitals contribute electronic states below the CBM, while Tl^+-6s* orbitals populate states above the VBM, effectively reducing the band gap. Hence, Tl^+ serves as a two-level activator by taking the position of its two antibonding states inside the band gap of the host compound Cs_4SrI_6. The investigation of optical properties, namely, dielectric function, refractive index, and absorption coefficient indicates that the electron transfer from the Tl^+-6s* and Tl^+-6s states to the Tl^+-6p* state becomes progressively strong with the increase in Tl^+-dopant concentration. Moreover, electronic transitions originating from the VB, predominantly comprising I^--p states, reliably play a leading role in transitions to both the Tl^+-6p*-controlled split CB and the Sr^{2+}-d-controlled CB. Owing to the existence of the Tl^+-6p* atomic orbital and Tl^+-6s* atomic orbital within the band gap, Tl^+ can be involved in multiple excitation and subsequent de-excitation through $6s^2 \leftrightarrow 6s^1p^1$ transition, providing a major involvement in the total light output in addition to excitonic and defect-assisted luminescence as observed in NaI:Tl scintillators.

Moreover, core-level transitions associated with the Tl^+-6s orbital play a crucial role in tailoring the opto-electronic response by converting Auger-assisted cross-luminescence into Auger-free cross-luminescence, enhancing the radiative efficiency in the Tl^+-doped Cs_4SrI_6 scintillator. Furthermore, the values of radiant quantum efficiency are 39.52%, 41.41%, and 43.70% for Cs_4SrI_6 doped with 1.52% Tl^+, 3.03% Tl^+, and 4.55% Tl^+, respectively. The undoped Cs_4SrI_6 sample was excluded from the QE analysis due to the unknown emission peak energy. In addition, the theoretical upper limit of LY for pure, 1.52%, 3.03% and 4.55% Tl^+-doped Cs_4SrI_6 structures is anticipated at 97 324 photons per MeV, 100 503 photons per MeV, 102 564 photons per MeV and 108 401 photons per MeV, respectively. In addition, this investigation reveals that the Auger luminescence in pure Cs_4SrI_6 is converted into an Auger-free luminescence process after Tl^+ doping, which consequently reduces self-absorption losses. While higher Tl^+-dopant concentrations may improve the performance under ideal conditions, practical implementations are often limited by concentration quenching at higher dopant levels, which can adversely affect the overall scintillation performance. However, the findings suggest that the Tl^+ dopant can enhance the scintillation activities of the compound Cs_4SrI_6 by initiating additional electron transfer and their radiative recombination channels. In addition, the dependence on rare-earth activators, which typically produce characteristic scintillation *via* allowed $4f^n \leftrightarrow 4f^{n-1}5d$ electronic transitions like Eu^{2+}, can be significantly reduced. It is believed that this research will provide a deeper insight into the underlying physical mechanism and guide the design of a more effective Cs_4SrI_6 scintillator, where Tl^+ will act as a two-level activator for the characteristic and well-defined single-peak emission.

Consent for publication

All authors of this work have agreed and are ready to sign the Transfer of Copyright which empowers the Publisher to protect the work against unauthorized use and to maintain the integrity of the work from a bibliographical and archival standpoint.

Author contributions

Md. Helal Miah: literature review, performing the study, data curation, data analysis and writing of the original draft. Yahaya Saadu Itas, Amran Hossain, Phannee Saengkaew, Arshid Numan, Mohammad Nur-E-Alam, and Mohammad Aminul Islam: data curation, discussion, software and validation. Mayeen Uddin Khandaker: conceptualization, supervision, and reviewing and editing of the manuscript.

Conflicts of interest

The authors declare no known competing interests that could have appeared to influence the work reported in this paper.

Data availability

All data are available in the manuscript.

Acknowledgements

The Sunway University Scholarship support received by Md. Helal Miah is acknowledged. During the preparation of this work, the authors used some online services (such as Grammarly and Gemini) in order to improve the language and readability. After using this tool/service, the authors reviewed and edited the content as needed and took full responsibility for the content of the publication.

References

1 H. Lusic and M. W. Grinstaff, X-ray-computed tomography contrast agents, *Chem. Rev.*, 2013, **113**(3), 1641–1666, DOI: 10.1021/CR200358S.
2 Y. Wang, Intuitive dimensional analyses of the energy and atomic number dependences of the cross sections for radiation interaction with matter, *J. Xray Sci. Technol.*, 2007, **15**(3), 169–175, DOI: 10.3233/XST-2007-00177.
3 D. R. White, An analysis of the Z-dependence of photon and electron interactions, *Phys. Med. Biol.*, 1977, **22**(2), 219, DOI: 10.1088/0031-9155/22/2/003.
4 Md. H. Miah, M. U. Khandaker, P. Saengkaew, A. Numan and M. A. Islam, Advances in perovskite-based scintillation materials for gamma-ray spectroscopy: issues and

opportunities, *RSC Adv.*, 2025, **15**(51), 43446–43486, DOI: 10.1039/D5RA04980F.
5 S. Stave, Germanium Detectors in Homeland Security at PNNL, *J. Phys. Conf. Ser.*, 2015, **606**(1), 012018, DOI: 10.1088/1742-6596/606/1/012018.
6 K. S. Pestovich, L. Stand, C. L. Melcher, E. Van Loef and M. Zhuravleva, Crystal growth of new high light yield halide perovskite scintillator RbSrI3, *J. Cryst. Growth*, 2024, **627**, 127540, DOI: 10.1016/J.JCRYSGRO.2023.127540.
7 M. A. K. Sheikh, *et al.*, Solution-Processable A2XY4 (A = PEA, BA; X = Pb, Sn, Cu, Mn; Y = Cl, Br, I) Crystals for High Light Yield and Ultrafast Scintillators, *IEEE Trans. Nucl. Sci.*, 2023, **70**(7), 1384–1391, DOI: 10.1109/TNS.2023.3267636.
8 K. S. Pestovich, L. Stand, C. L. Melcher, E. Van Loef and M. Zhuravleva, Crystal growth of new high light yield halide perovskite scintillator RbSrI3, *J. Cryst. Growth*, 2024, **627**, 127540, DOI: 10.1016/J.JCRYSGRO.2023.127540.
9 S. González-Carrero, R. E. Galian and J. Pérez-Prieto, Organometal Halide Perovskites: Bulk Low-Dimension Materials and Nanoparticles, *Part. Part. Syst. Char.*, 2015, **32**(7), 709–720, DOI: 10.1002/PPSC.201400214.
10 D. Liu, H. Zeng, H. Peng and R. Sa, Computational study of the fundamental properties of Zr-based chalcogenide perovskites for optoelectronics, *Phys. Chem. Chem. Phys.*, 2023, **25**(19), 13755–13765, DOI: 10.1039/d3cp01522j.
11 V. Vasylkovskyi, I. Bespalova, M. Slipchenko, O. Slipchenko, Y. Zholudov and B. Chichkov, Review: Electrochemiluminescence of Perovskite-Related Nanostructures, *Crystals*, 2023, **13**(3), 455, DOI: 10.3390/CRYST13030455.
12 J. Shamsi, A. S. Urban, M. Imran, L. De Trizio and L. Manna, Metal Halide Perovskite Nanocrystals: Synthesis, Post-Synthesis Modifications, and Their Optical Properties, *Chem. Rev.*, 2019, **119**(5), 3296–3348, DOI: 10.1021/ACS.CHEMREV.8B00644/ASSET/IMAGES/MEDIUM/CR-2018-00644B_0057.GIF.
13 L. Stand, *et al.*, Crystal Growth and Scintillation Properties of Eu2+ doped Cs4CaI6 and Cs4SrI6, *J. Cryst. Growth*, 2018, **486**, 162–168, DOI: 10.1016/J.JCRYSGRO.2018.01.017.
14 D. Rutstrom, L. Stand, M. Koschan, C. L. Melcher and M. Zhuravleva, Europium concentration effects on the scintillation properties of Cs4SrI6:Eu and Cs4CaI6:Eu single crystals for use in gamma spectroscopy, *J. Lumin.*, 2019, **216**, 116740, DOI: 10.1016/J.JLUMIN.2019.116740.
15 D. Rutstrom, L. Stand, B. Dryzhakov, M. Koschan, C. L. Melcher and M. Zhuravleva, Crystal growth and scintillation properties of new ytterbium-activated scintillators Cs4CaI6:Yb and Cs4SrI6:Yb, *Opt. Mater.*, 2020, **110**, 110536, DOI: 10.1016/J.OPTMAT.2020.110536.
16 E. M. Becker and A. T. Farsoni, Wireless, low-cost, FPGA-based miniature gamma ray spectrometer, *Nucl. Instrum. Methods Phys. Res. A*, 2014, **761**, 99–104, DOI: 10.1016/J.NIMA.2014.05.096.
17 M. Gascón, H. Álvarez-Pol, J. Benlliure, E. Casarejos, D. Cortina-Gil and I. Durán, Optimization of energy resolution obtained with CsI(Tl) crystals for the R3B calorimeter, *IEEE Trans. Nucl. Sci.*, 2008, **55**(3), 1259–1262, DOI: 10.1109/TNS.2008.922808.
18 E. Sakai, Recent measurements on scintillator-photodetector systems, *IEEE Trans. Nucl. Sci.*, 1987, **34**(1), 418–422, DOI: 10.1109/TNS.1987.4337375.
19 R. Hawrami, E. Ariesanti, A. Farsoni, D. Szydel and H. Sabet, Growth and Evaluation of Improved CsI:Tl and NaI:Tl Scintillators, *Crystals*, 2021, **12**(11), 1517, DOI: 10.3390/CRYST12111517.
20 K. Yang and P. R. Menge, Improving γ-ray energy resolution, non-proportionality, and decay time of NaI:Tl+ with Sr2+ and Ca2+ co-doping, *J. Appl. Phys.*, 2015, **118**(21), 213106, DOI: 10.1063/1.4937126.
21 D. Liu, H. Zeng, H. Peng and R. Sa, A theoretical exploration of the structural feature, mechanical, and optoelectronic properties of Au-based halide perovskites A2AuIAuIIIX6 (A = Rb, Cs; X = Cl, Br, I), *Phys. Chem. Chem. Phys.*, 2023, **25**(42), 28974–28981, DOI: 10.1039/d3cp04269c.
22 P. Giannozzi, *et al.*, Advanced capabilities for materials modelling with Quantum ESPRESSO, *J. Phys.: Condens. Matter*, 2017, **29**(46), 465901, DOI: 10.1088/1361-648X/AA8F79.
23 Y. Wu, *et al.*, Zero-dimensional Cs4EuX6 (X = Br, I) all-inorganic perovskite single crystals for gamma-ray spectroscopy, *J. Mater. Chem. C Mater*, 2018, **6**(25), 6647–6655, DOI: 10.1039/C8TC01458B.
24 J. P. Perdew, K. Burke and M. Ernzerhof, Generalized Gradient Approximation Made Simple, *Phys. Rev. Lett.*, 1996, **77**(18), 3865, DOI: 10.1103/PhysRevLett.77.3865.
25 M. H. Miah, Y. S. Itas, P. Saengkaew, M. A. Islam and M. U. Khandaker, First-principles study of high-performance scintillators: Tl-doping in CsSrI3 perovskite, *Mater. Chem. Phys.*, 2026, **348**, 131532, DOI: 10.1016/J.MATCHEMPHYS.2025.131532.
26 H. Ahmad, A. Rauf, A. Ahmad, A. Ulhaq and S. Muhammad, First-principles study on the electronic and optical properties of Bi2WO6, *RSC Adv.*, 2021, **11**(51), 32330–32338, DOI: 10.1039/d1ra03784f.
27 G. Prandini, M. Galante, N. Marzari and P. Umari, SIMPLE code: Optical properties with optimal basis functions, *Comput. Phys. Commun.*, 2019, **240**(11), 106–119, DOI: 10.1016/j.cpc.2019.02.016.
28 M. H. Miah, *et al.*, First-principles study of the structural, mechanical, electronic, optical, and elastic properties of non-toxic XGeBr3 (X=K, Rb, and Cs) perovskite for optoelectronic and radiation sensing applications, *Mater. Chem. Phys.Jun*, 2024, **319**, 129377, DOI: 10.1016/j.matchemphys.2024.129377.
29 F. Herman, The Electronic Energy Band Structure of Silicon and Germanium, *Proc. IRE*, 1955, **43**(12), 1703–1732, DOI: 10.1109/JRPROC.1955.278039.
30 A. Wacker, *An Introduction to the Concept of Band Structure*, 2010.
31 Z. Jellil, H. Jebari, A. Soussi, M. Eddekkar, A. Aboulkassim and H. Ez-Zahraouy, Analysis of the structural, electronic, optical and mechanical properties of CsGeI2Br under tensile and compressive strain for optoelectronic

applications: A DFT computational perspective, *Micro Nanostruct.*, 2024, **186**, 207750, DOI: 10.1016/J.MICRNA.2023.207750.

32 Z. Zhang, Q. Zhao, Y. Li and X. P. Ouyang, Electronic structure and optical properties of CsI, CsI(Ag), and CsI(Tl), *J. Korean Phys. Soc.*, 2016, **68**(9), 1069–1074, DOI: 10.3938/JKPS.68.1069/METRICS.

33 Q. Li, R. T. Williams and D. Åberg, First principles calculations and experiment predictions for iodine vacancy centers in SrI2, *Phys. Status Solidi B*, 2013, **250**(2), 233–243, DOI: 10.1002/PSSB.201200503.

34 H. Shi and M. H. Du, Discrete Electronic Bands in Semiconductors and Insulators: Potential High-Light-Yield Scintillators, *Phys. Rev. Appl.*, 2015, **3**(5), 054005, DOI: 10.1103/PHYSREVAPPLIED.3.054005/FIGURES/7/THUMBNAIL.

35 D. Liu, H. Peng, J. He and R. Sa, Alloy engineering to tune the optoelectronic properties and photovoltaic performance for Hf-based chalcogenide perovskites, *Mater. Sci. Semicond. Process.*, 2024, **169**(17), 107919, DOI: 10.1016/j.mssp.2023.107919.

36 B. Chen, R. Chen and B. Huang, Strong Electron–Phonon Coupling Induced Self-Trapped Excitons in Double Halide Perovskites, *Adv. Energy Sustain. Res.*, 2023, **4**(9), 2300018, DOI: 10.1002/aesr.202300018.

37 M. H. Du, Chemical trends of electronic and optical properties of ns2 ions in halides, *J. Mater. Chem. C Mater*, 2014, **2**(24), 4784–4791, DOI: 10.1039/C4TC00485J.

38 M. E. El Sayed, S. Naji, M. N. Murshed and A. Samir, Cation substitution for tunable electronic, optical and scintillation properties of Pb1-xCaxWO4 materials: A density functional theory study, *Results Phys.*, 2021, **30**, 104826, DOI: 10.1016/J.RINP.2021.104826.

39 A. Zaghrane, *et al.*, Comprehensive investigation of Rb2LuCl5 and Rb2PrCl5 rare earth-based scintillation materials using density functional theory, *Mater. Res. Bull.*, 2025, **181**, 113071, DOI: 10.1016/J.MATERRESBULL.2024.113071.

40 S. Kubota, J. zhi Ruan (Gen), M. Itoh, S. Hashimoto and S. Sakuragi, A new type of luminescence mechanism in large band-gap insulators: Proposal for fast scintillation materials, *Nucl. Instrum. Methods Phys. Res. A*, 1990, **289**(1–2), 253–260, DOI: 10.1016/0168-9002(90)90267-A.

41 Z. Jellil, *et al.*, Band gap shifting of halide perovskite KSrCl3 from ultra-violet to visible region under pressure for photovoltaic applications, *Micro Nanostruct.*, 2024, **193**, 207911, DOI: 10.1016/J.MICRNA.2024.207911.

42 M. Eddekkar, *et al.*, Optimizing Cs2AgXCl6 (X=Bi, In) double perovskites for light-harvesting devices, *Mater. Today Commun.*, 2024, **40**, 109449, DOI: 10.1016/J.MTCOMM.2024.109449.

43 M. Catti, Crystal elasticity and inner strain: a computational model, *Acta Crystallogr., Sect. A:Found. Crystallogr.*, 1989, **45**(1), 20–25, DOI: 10.1107/S0108767388008748.

44 M. Taoufiq, *et al.*, Theoretical DFT and experimental investigation of the effect of Co doping in electrochemically deposited ZnSe films, *Opt. Mater.*, 2024, **155**, 115893, DOI: 10.1016/J.OPTMAT.2024.115893.

45 X. Liu, *et al.*, A high dielectric constant non-fullerene acceptor for efficient bulk-heterojunction organic solar cells, *J. Mater. Chem. A Mater*, 2018, **6**(2), 395–403, DOI: 10.1039/C7TA10136H.

46 D. R. Penn, Wave-Number-Dependent Dielectric Function of Semiconductors, *Phys. Rev.*, 1962, **128**(5), 2093, DOI: 10.1103/PhysRev.128.2093.

47 P. Ma, *et al.*, A 7-kW narrow-linewidth fiber amplifier assisted by optimizing the refractive index of the large-mode-area active fiber, *High Power Laser Sci. Eng.*, 2024, **12**, e67, DOI: 10.1017/HPL.2024.41.

48 M. N. Murshed, M. E. El Sayed, S. Naji and A. Samir, Electronic and optical properties and upper light yield estimation of new scintillating material TlMgCl3: Ab initio study, *Results Phys.*, 2021, **29**, 104695, DOI: 10.1016/J.RINP.2021.104695.

49 H. Ouhenou, *et al.*, Exploring the Cs2LiLuCl6 elpasolite scintillator for thermal-neutron detection: A comprehensive DFT and TD-DFT studies, *Radiat. Meas.*, 2024, **177**, 107228, DOI: 10.1016/J.RADMEAS.2024.107228.

50 K. Biswas and M. H. Du, Energy transport and scintillation of cerium-doped elpasolite Cs 2LiYCl 6: Hybrid density functional calculations, *Phys. Rev. B Condens. Matter Mater. Phys.*, 2012, **86**(1), 014102, DOI: 10.1103/PHYSREVB.86.014102/FIGURES/7/THUMBNAIL.

51 A. Canning and A. Chaudhry, First-principles study of luminescence in Ce-doped inorganic scintillators, *Phys. Rev. B Condens. Matter Mater. Phys.*, 2011, **83**(12), 125115, DOI: 10.1103/PhysRevB.83.125115.

52 P. W. M. Jacobs, Alkali halide crystals containing impurity ions with the ns2 ground-state electronic configuration, *J. Phys. Chem. Solids*, 1991, **52**(1), 35–67, DOI: 10.1016/0022-3697(91)90059-9.

53 M. H. Du, Chemical trends of electronic and optical properties of ns 2 ions in halides, *J. Mater. Chem. C*, 2014, 4784–4791, DOI: 10.1039/c4tc00485j.

54 M. M. Hamadaa, F. E. Costa, M. C. C. Pereira and S. Kubota, Dependence of scintillation characteristics in the CsI(Tl) crystal on Tl+ concentrations under electron and alpha particles excitations, *IEEE Nuclear Science Symposium and Medical Imaging Conference*, 2000, **1**, 1148–1153, DOI: 10.1109/NSSMIC.2000.949150.

55 K. Yang and P. R. Menge, Improving γ-ray energy resolution, non-proportionality, and decay time of NaI:Tl+ with Sr2+ and Ca2+ co-doping, *J. Appl. Phys.*, 2015, **118**(21), 213106, DOI: 10.1063/1.4937126/140289.

56 H. Kim, A. Khan, J. Daniel, G. Rooh and P. Q. Vuong, Thallium-based heavy inorganic scintillators: recent developments and future perspectives, *CrystEngComm*, 2022, **24**(3), 450–464, DOI: 10.1039/D1CE01422F.

57 W. Chevajarassakul, *et al.*, The impact of strontium composition on thallium-doped cesium iodide scintillators, *Nucl. Instrum. Methods Phys. Res. A*, 2023, **1057**, 168731, DOI: 10.1016/J.NIMA.2023.168731.

58 P. Saengkaew, *et al.*, Impact of precursor purity on optical properties and radiation detection of CsI:Tl scintillators, *Appl. Phys. A*, 2016, **122**(8), 729, DOI: 10.1007/S00339-016-0254-X.

59 V. Nagirnyi, S. Zazubovich, V. Zepelin, M. Nikl and G. P. Pazzi, A new model for the visible emission of the CsI: Tl crystal, *Chem. Phys. Lett.*, 1994, **227**(4–5), 533–538, DOI: 10.1016/0009-2614(94)00857-4.

60 Y. Yoshikawa, T. Kato, D. Nakauchi, N. Kawaguchi and T. Yanagida, Scintillation property of Tl-doped NaI transparent ceramics, *Radiat. Phys. Chem.*, 2024, **215**, 111367, DOI: 10.1016/j.radphyschem.2023.111367.

61 K. Miyazaki, D. Nakauchi, T. Kato, N. Kawaguchi and T. Yanagida, Tl-concentration dependence of photoluminescence and scintillation properties in Tl-doped RbI single crystals, *J. Mater. Sci.: Mater. Electron.*, 2022, **33**(28), 22162–22168, DOI: 10.1007/s10854-022-08996-y.

62 D. J. Robbins, On Predicting the Maximum Efficiency of Phosphor Systems Excited by Ionizing Radiation, *J. Electrochem. Soc.*, 1980, **127**(12), 2694–2702, DOI: 10.1149/1.2129574/XML.

63 H. Shi and M. H. Du, Discrete Electronic Bands in Semiconductors and Insulators: Potential High-Light-Yield Scintillators, *Phys. Rev. Appl.*, 2015, **3**(5), 054005, DOI: 10.1103/PHYSREVAPPLIED.3.054005/FIGURES/7/THUMBNAIL.

64 P. Dorenbos, Light output and energy resolution of Ce3+-doped scintillators, *Nucl. Instrum. Methods Phys. Res., Sect. A*, 2002, **486**(1–2), 208–213, DOI: 10.1016/S0168-9002(02)00704-0.

65 P. A. Rodnyi, P. Dorenbos and C. W. E. van Eijk, Energy Loss in Inorganic Scintillators, *Phys. Status Solidi B*, 1995, **187**(1), 15–29, DOI: 10.1002/PSSB.2221870102.

66 A. Lempicki, A. J. Wojtowicz and E. Berman, Fundamental limits of scintillator performance, *Nucl. Instrum. Methods Phys. Res. A*, 1993, **333**(2–3), 304–311, DOI: 10.1016/0168-9002(93)91170-R.

67 G. Blasse, Reviews: Scintillator Materials, *Chem. Mater.*, 1994, **6**(9), 1465–1475, DOI: 10.1021/CM00045A002/ASSET/CM00045A002.FP.PNG_V03.

68 A. Xie, *et al.*, Thermal Quenching and Dose Studies of X-ray Luminescence in Single Crystals of Halide Perovskites, *J. Phys. Chem. C*, 2018, **122**(28), 16265–16273, DOI: 10.1021/ACS.JPCC.8B03622/SUPPL_FILE/JP8B03622_SI_002.CIF.

69 J. J. van Blaaderen, C. van Aarle, D. Leibold, P. Dorenbos and D. R. Schaart, Guidelines for the Selection of Scintillators for Indirect Photon-Counting X-ray Detectors, *Chem. Mater.*, 2025, **37**, 1716–1740, DOI: 10.1021/ACS.CHEMMATER.4C03437.

70 M. Moszyński, R. Allemand and M. Laval, *Recent Progress in Fast Timing with CsF Scintillators in Application to Time-Of-Flight Positron Tomography in Medicine*, Elsevier, 1983, Accessed: Apr. 01, 2025. [Online]. Available: https://www.sciencedirect.com/science/article/pii/0167508783901941.

71 J. Jansons, *et al.*, Cross-luminescence of complex halide crystals, *J. Phys.: Condens. Matter*, 1993, **5**(10), 1589, DOI: 10.1088/0953-8984/5/10/015.

72 V. Khanin, I. Venevtsev and P. Rodnyi, Recent advances in the study of core-valence luminescence (cross luminescence). Review, *Opt. Mater.*, 2023, **136**, 113399, DOI: 10.1016/J.OPTMAT.2022.113399.

73 C. W. E. van Eijk, Cross-luminescence, *J. Lumin.*, 1994, **60–61**(C), 936–941, DOI: 10.1016/0022-2313(94)90316-6.

74 T. Yanagida and T. Yamazaki, Inorganic scintillating materials and scintillation detectors, *Proc. Jpn. Acad. B Phys. Biol. Sci.*, 2018, **94**(2), 75–97, DOI: 10.2183/PJAB.94.007.

75 P. A. Rodnyi, Core–valence luminescence in scintillators, *Radiat. Meas.*, 2004, **38**(4–6), 343–352, DOI: 10.1016/j.radmeas.2003.11.003.

76 G. Shwetha and V. Kanchana, Optical isotropy in structurally anisotropic halide scintillators: Ab initio study, *Phys. Rev. B Condens. Matter Mater. Phys.*, 2012, **86**(11), 115209, DOI: 10.1103/PHYSREVB.86.115209/FIGURES/9/THUMBNAIL.

77 T. Yanagida and T. Yamazaki, Inorganic scintillating materials and scintillation detectors, *Proc. Jpn. Acad. B Phys. Biol. Sci.*, 2018, **94**(2), 75–97, DOI: 10.2183/PJAB.94.007.